

Integrated ytterbium gain for visible-near-infrared photonics

Tianyi Zeng,^{1,*} Erik W. Masselink,^{1,2,*} Tsung-Han Wu,^{3,4} Nathan Brooks,⁴ Peter Chang,⁴ Grisha Spektor,⁵ Zachary L. Newman,⁵ Danxian Liu,¹ Scott B. Papp,^{6,7} David R. Carlson,⁵ Scott A. Diddams,^{3,7} and Kiyoul Yang^{1,†}

¹*John A. Paulson School of Engineering and Applied Sciences, Harvard University*

²*Department of Electrical Engineering and Computer Science, Massachusetts Institute of Technology*

³*Electrical, Computer and Energy Engineering, University of Colorado, Boulder*

⁴*Chi3 Optics LLC, Boulder, CO, USA*

⁵*Octave Photonics, Louisville, CO, USA*

⁶*Time and Frequency Division, National Institute of Standards and Technology, Boulder, CO, USA*

⁷*Department of Physics, University of Colorado Boulder*

Rare-earth gain media [1, 2] form the foundation of modern optical communications, emerging quantum hardware [3, 4], and ultrafast optics [5–7]. While chip-scale integration can enable fiber-like – and potentially beyond-fiber – functionality with unprecedented scalability, development in the visible and near-infrared remains in its early stages. Here, we demonstrate ytterbium-based optical gain integrated into an aluminum oxide photonic platform, achieving both single-mode lasing and optical amplification in the near-infrared regime. This platform delivers optical amplification with output powers exceeding 0.5 W, an optical-to-optical conversion efficiency above 70%, and a noise figure of 3.3 dB, approaching the quantum limit for phase-insensitive amplification. Furthermore, we achieve femtosecond pulse amplification to a record peak power of 14 kW, enabling supercontinuum generation with visible dispersive waves extending from 780 to 476 nm in conjunction with nonlinear photonic devices. This platform is compatible with heterogeneous integration into standard photonic circuits, laying the foundation for scalable visible-near-infrared photonic systems, including coherent laser arrays, mode-locked lasers [8, 9], optical clocks [10, 11], and microwave oscillators [12, 13].

I. INTRODUCTION

Rare-earth-based optical amplifiers and lasers [1, 2, 14] are foundational to modern science and technology, most notably serving as the backbone of global optical communications. They underpin a broad range of frontier scientific explorations (Fig. 1a) – particularly at short near-infrared (NIR) and visible wavelengths – including neutral-atom quantum processors [4, 15], manipulation of ultracold molecules [3, 16], nonlinear microscopy in neuroscience [17], and precision spectroscopy in astronomical observatories [5, 18, 19]. The rapid adoption of rare-earth-doped, particularly ytterbium-doped, fiber systems across these visible-NIR regimes is directly driven by their unparalleled performance metrics: high output power and high optical-to-optical conversion efficiency, low noise figure, broad gain bandwidth, and low thermal load. Incorporating rare-earth ions into thin-film waveguides has been widely explored as scalable gain platforms, using a range of dopants including erbium, ytterbium, neodymium, and thulium, in host materials such as silica, aluminum oxide, lithium niobate, silicon nitride, tantalum pentoxide, and tellurium oxide [20–32]. However, as integrated photonics has expanded into the visible and NIR regimes [33–36], the successful incorporation of rare-earth-based gain and light sources in this wavelength range remains a critical, unresolved challenge.

This work presents the integration of Yb-based

optical gain for visible-NIR photonics, leveraging two fundamental physical advantages. First, the simple energy-level structure of Yb³⁺ ions (Fig. 1b) facilitates high output power and optical-to-optical conversion efficiency in the NIR [14]. The corresponding reduction in thermal load is critical, as heat dissipation and its associated thermorefractive noise remain primary bottlenecks in integrated photonics [37–40]. Second, the Yb gain band (1010 nm - 1090 nm) lies near the edge of the anomalous dispersion window in integrated nonlinear platforms. Consequently, ultrafast pulses generated and amplified within this band can undergo spectral broadening to reach – and potentially fully encompass – the visible wavelength range. We integrate Yb³⁺ ions into a low-loss aluminum oxide (AlO_x, hereafter alumina) platform [20, 23, 41], enabling the integration of a wide range of on-chip photonic components, material systems, as well as CMOS electronics [34, 42–46].

Using this platform, we demonstrate low-noise continuous-wave amplification with efficiencies exceeding 70%, along with ultrafast pulse amplification to nanojoule-level energies and 14 kW peak power after compression. These high-energy pulses drive supercontinuum generation from the NIR into the blue, establishing an integrated route toward short NIR and visible light generation (Fig. 1a).

II. DESIGN AND FABRICATION

Alumina is well-suited as a host material due to its high rare-earth solubility [27], wide bandgap, and low optical nonlinearity [49, 50]. To the best of our

* These authors contributed equally to this work.

† kiyoul@seas.harvard.edu

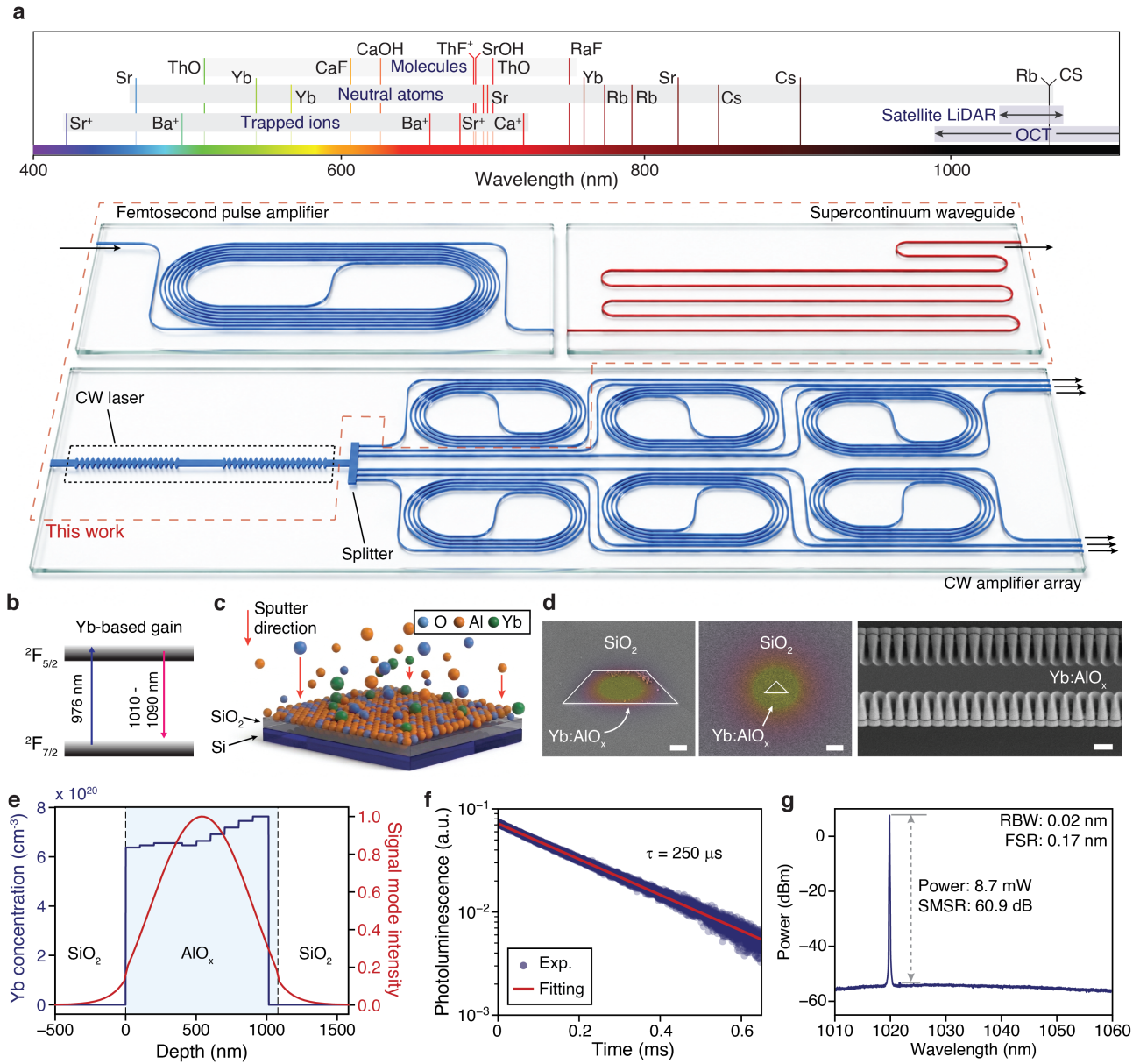


FIG. 1. Integrated ytterbium-doped alumina photonic platform. (a) **Top:** Spectrum coverage in the visible to short NIR regions, illustrating wavelength requirements for various photonic applications and physical systems [3, 4, 10, 16, 47, 48]. **Bottom:** Schematics of two photonic systems incorporating Yb:AlO_x amplifiers. The first consists of a pulse amplifier followed by a nonlinear waveguide for supercontinuum generation. The second system consists of a CW amplifier array seeded by a master single-mode laser. (b) A simplified energy-level diagram of the Yb³⁺ ions in alumina, with pumping at 976 nm (as used in this work) and the signal wavelengths spanning from 1010 to 1090 nm. (c) Schematic of the co-sputtering process for depositing a Yb:AlO_x film onto an oxidized silicon substrate. (d) SEM images, from left to right: cross-sectional images of the amplifier waveguide, amplifier facet and a top view of the Bragg reflector for the DFB laser. Simulations of the signal modes are overlaid. All scale bars in this panel are 500 nm. (e) Vertical profiles of the measured dopant concentration (characterized by RBS) and the simulated optical TE₀₀-mode intensity across the waveguide center. (f) Measured photoluminescence decay from the ²F_{5/2} manifold, with a fitted curve overlaid, showing a lifetime of 250 μs. (g) Measured output optical spectrum of a Yb:AlO_x single-mode DFB laser. OSA resolution bandwidth (RBW): 0.02 nm; cavity free spectral range (FSR): 0.17 nm.

knowledge, amorphous alumina films have not been reported to exhibit photorefractive effects, in contrast to crystalline materials [51, 52], consistent with our observation in this work. We employ the co-sputtering technique (Fig. 1c) that has been established for rare-

earth-doped alumina photonic circuits [23, 27, 31, 53]. The highest process temperature in this work is 725 °C, used to anneal the top cladding rather than the alumina film. However, sputtered alumina has been demonstrated with processing temperatures as low as 150 °C [41],

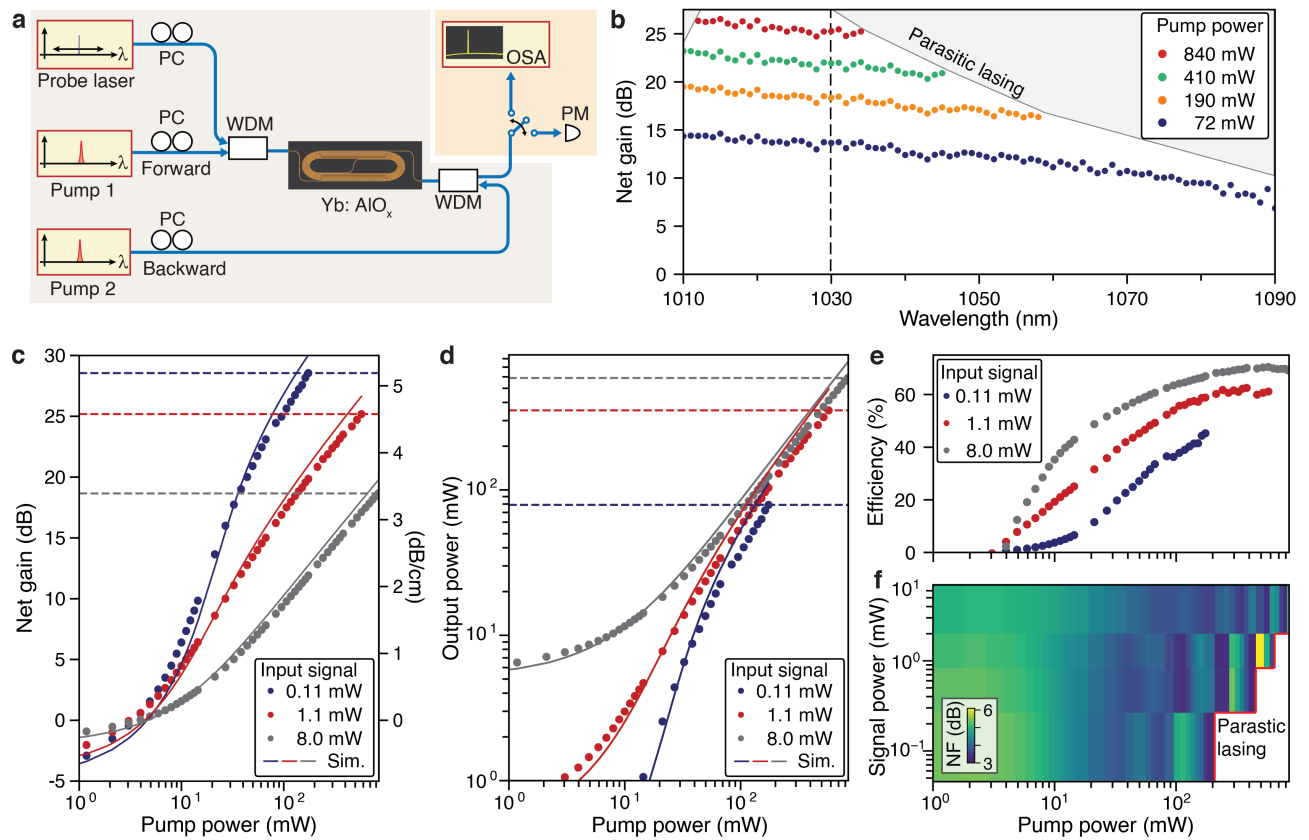


FIG. 2. **CW optical amplification.** (a) Experimental setup for CW optical amplification with bidirectional pumping (pump 1 and 2) and a tunable probe laser. PC, polarization controller; OSA, optical spectrum analyzer; PM, power meter; WDM, wavelength division multiplexer. (b) Measured gain spectra at different pump powers; the gray shaded region marks the onset and parameter space of parasitic lasing. (c-d) Measured data (points) and simulations (lines) of the on-chip net gain (c) and output power (d) at 1030 nm. (e) Measured optical-to-optical conversion efficiency as a function of pump power for different signal powers. (f) Measured noise figure. The red contour indicates the onset of parasitic lasing. (e-f) share a common horizontal axis and were measured at 1030 nm.

potentially enabling compatibility with back-end-of-line passive photonics foundry processes [54].

The co-sputtering process enables uniform dopant incorporation throughout the 1.08- μm -thick waveguide cores without inducing surface damage, resulting in a root-mean-square top-surface roughness of 120 pm, as measured by atomic force microscopy. After film growth, the waveguides were patterned lithographically and etched with reactive ion etching, followed by top-cladding deposition and annealing. The passive waveguide loss is 9.7 dB/m at 1060 nm and is dominated by etch-induced sidewall roughness. To reduce reflections and fiber-coupling loss, the waveguides were designed with 3D inverse tapers in both height and width, implemented in a single lithography and etching step, yielding a coupling loss of 1.0 dB per facet (characterization of passive and coupling loss in Supplementary Information). Cross-sectional scanning electron microscope (SEM) images are shown in Fig. 1d.

The resulting film was characterized by Rutherford backscattering spectrometry (RBS; Fig. 1e) and exhibits a Yb^{3+} concentration of 6.8×10^{20} atoms/ cm^3 ,

corresponding to 0.76 at.% (atomic percentage) and 62,000 ppm by weight in the doped alumina layer. The high concentration is enabled by the low quenching of Yb^{3+} due to its simple energy-level structure [14]. The luminescence lifetime of the Yb^{3+} ions was measured to be 250 μs by intensity-modulating the pump and monitoring the amplified spontaneous emission from the ytterbium-doped alumina waveguide (Fig. 1f). The lifetime is shorter than the typical 1 ms lifetime observed in Yb-doped fibers [55] due to the high doping concentration, but agrees with recent measurements in highly doped sputtered alumina [56].

The Yb-doped alumina waveguides are clad with silica (SiO_2) and are designed with a height of 1.08 μm , a width of 1.50 μm , and a 52° sidewall angle, resulting in a mode area of 1.90 μm^2 . This geometry leads to a high pump-signal mode overlap of 97.7% and a doped region overlap factor of 89.5%. The doped region overlap factor denotes the fraction of the signal mode contained in the doped region [57], and is calculated using the dopant profile measured by RBS (Fig. 1e). Together, the large mode area, high doped region overlap factor, and highly

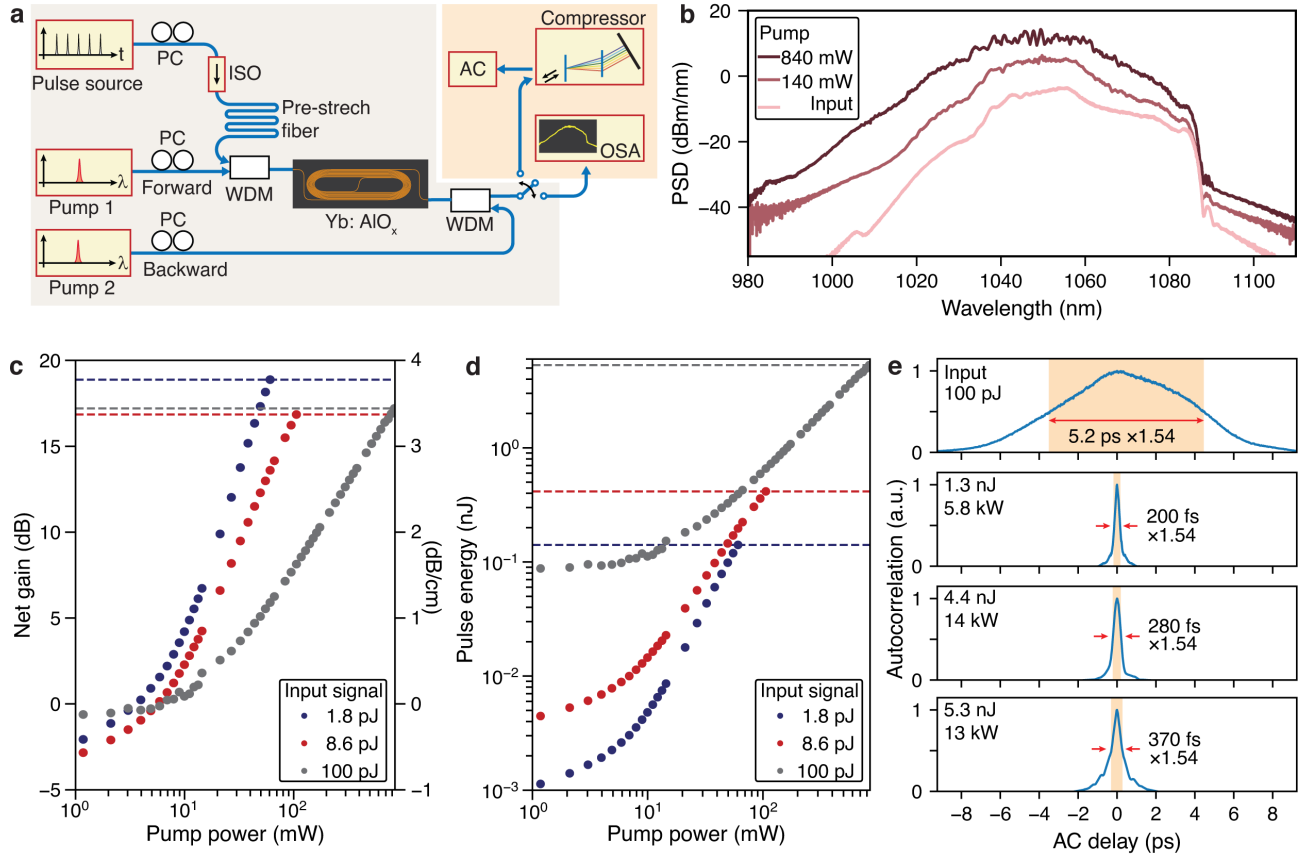


FIG. 3. **Femtosecond pulse amplification.** (a) Experimental setup for femtosecond pulse amplification with bidirectional pumping and a fiber-based pulse source. AC, autocorrelator; ISO, isolator. (b) Optical spectra of the on-chip input and amplified output at various pump powers for an input pulse energy of 100 pJ. (c-d) Measured net gain (c) and output pulse energy (d) at different input pulse energies. (e) Optical intensity autocorrelation (AC) traces of the pre-chirped input pulse (top) and the amplified output pulses. Pulse energies and peak powers are indicated in the upper-left corner of each subplot. The output traces were recorded after optimized linear chirp compression. The pulse widths were calculated using a deconvolution factor of 0.65, assuming a sech-squared pulse shape. All reported pulse energies and peak powers are on-chip.

confined mode enable low nonlinearity, high gain, and a compact, scalable footprint, respectively.

As a proof of concept, single-mode operation of a continuous-wave (CW) laser is demonstrated in Fig. 1g. The distributed feedback (DFB) laser consists of two Bragg reflectors (Fig. 1d) providing a 0.7-nm-wide reflection band centered at 1020 nm, with a Yb-doped waveguide between them. The laser cavity's free spectral range is 0.17 nm, extracted from the resonance spacing measured using a swept tunable laser. The device emits from both facets and delivers 8.7 mW of on-chip power per side, with a side-mode suppression ratio (SMSR) of 60.9 dB (see Supplementary Information).

III. CONTINUOUS-WAVE AMPLIFICATION

A 55-mm spiral amplifier was characterized under bidirectional 976-nm pumping (Fig. 2a). The pump and signal were combined for amplification and subsequently separated using 980/1060 nm wavelength-

division multiplexers (WDMs), and chip coupling was performed with ultra-high-numerical-aperture fibers (Nufern UHNA3). We measured the spectral response of the amplifier by sweeping the wavelength of the signal laser, keeping its on-chip power fixed at 1.7 mW. Optical gain was observed from 1010 to 1090 nm, with a peak net gain of 26.5 dB at 1015 nm (Fig. 2b). Measurements of higher gain were limited by parasitic lasing arising from facet reflections.

We further characterized CW amplification at a fixed wavelength of 1030 nm (Fig. 2c-f). This wavelength was selected to minimize parasitic lasing and reduce insertion loss in the fiber WDM. It is therefore not chosen for maximum gain. For a small-signal input power of 110 μ W at 1030 nm, we measured an on-chip net gain of 28.6 dB, corresponding to an off-chip net gain of 26.6 dB, accounting for the fiber-to-chip coupling loss of 1.0 dB per facet (Fig. 2c). The resulting gain coefficient is 5.2 dB/cm. In the large-signal regime, with an input power of 8.0 mW and a pump power of 840 mW, the maximum output power reaches 590 mW (Fig. 2d), corresponding to a gain of 18.7 dB.

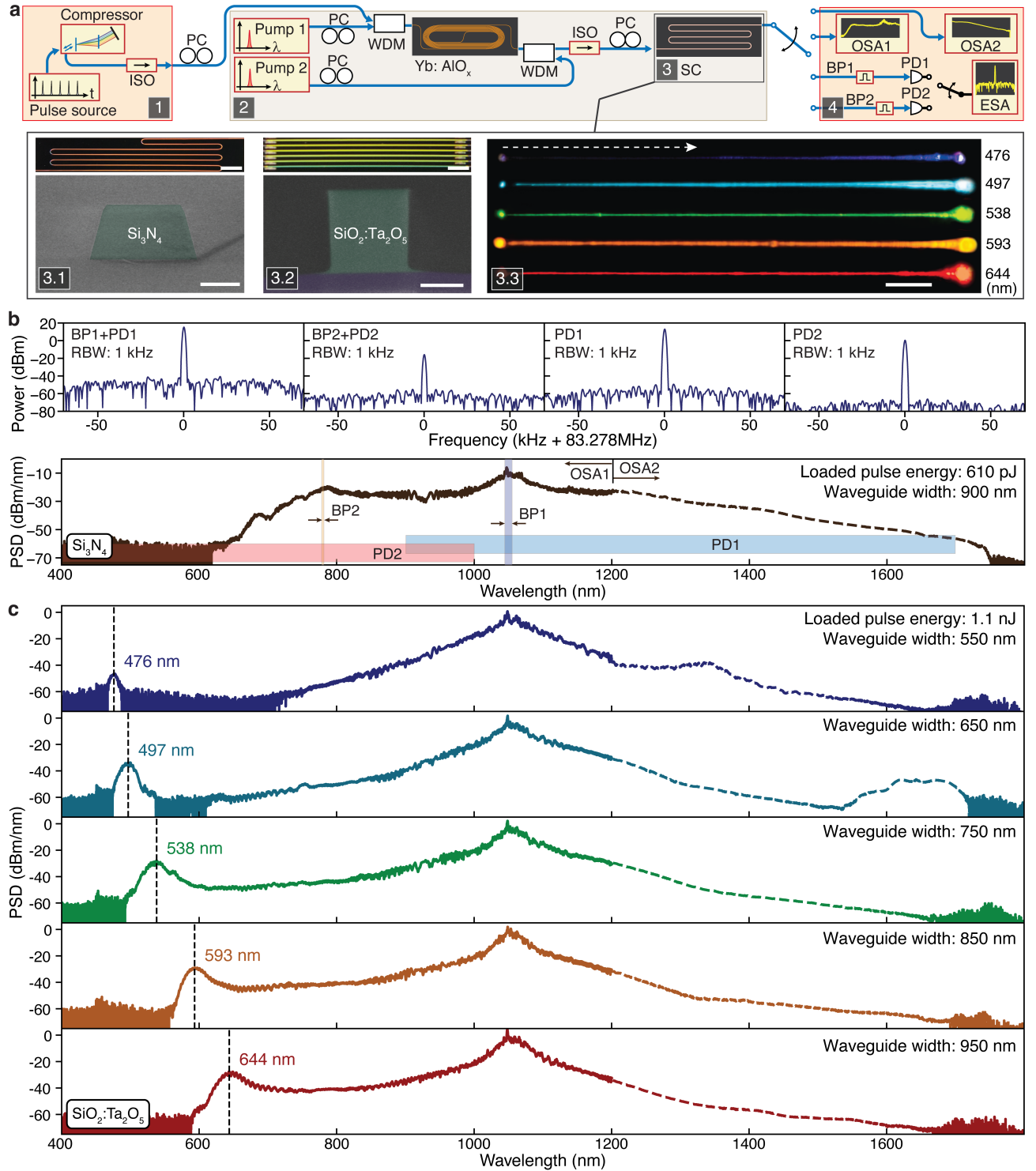


FIG. 4. **Visible-to-NIR supercontinuum generation.** (a) Experimental setup for supercontinuum generation: (1) Fiber-based pulse source with a free-space compressor and isolator for pre-chirped input. (2) Bidirectionally pumped femtosecond pulse amplifier. (3) Supercontinuum (SC) waveguide. (4) Output characterization setup including OSAs, photodetectors (PD) with bandpass filters (BP), and an electrical spectrum analyzer (ESA). Insets of (3): Optical top view and SEM cross-sections of Si_3N_4 (3.1) and $\text{SiO}_2:\text{Ta}_2\text{O}_5$ (3.2) waveguides, and a top-view photograph of waveguide arrays showing visible dispersive-wave generation in the $\text{SiO}_2:\text{Ta}_2\text{O}_5$ waveguides (3.3). Scale bars: 500 nm for the SEM images in panels (3.1)–(3.2), and 500 μm for all top views in panels (3.1)–(3.3). (b) Si_3N_4 supercontinuum spectrum, with narrow-band near-infrared (near-visible) comb lines filtered by BP1 (BP2) and detected by PD1 (PD2) for the repetition beatnotes shown above. Repetition beatnotes from the broadband optical signal measured by PD1 and PD2 without filters are also shown. (c) Supercontinuum spectra of the $\text{SiO}_2:\text{Ta}_2\text{O}_5$ waveguides with varying waveguide widths, showing the corresponding dispersive wave positions. All optical spectra were measured using two OSAs covering the full wavelength range of interest and stitched at 1200 nm.

A maximum efficiency of 71% is achieved at a lower pump power of 580 mW (Fig. 2e). The accompanying simulations are based on a two-level rate-equation model and agree qualitatively with our measurements (Fig. 2c–d). We used the model to extract an energy-transfer upconversion factor of 5×10^{-18} cm³/s and to calculate the minimum spontaneous emission factor and saturation energy discussed below.

We also measured the noise figure (NF), observing a minimum off-chip value of 4.3 dB that corresponds to an on-chip value of 3.3 dB (Fig. 2f). This value is very close to the 3.29 dB limit calculated from the minimum spontaneous emission factor (n_{sp}) of Yb³⁺. We note that asymmetric chip-to-fiber coupling at the two facets can bias the on-chip noise figure estimation. A discussion of coupling asymmetry, the rate equation model, and the minimum noise figure is provided in Supplementary Information.

IV. ULTRAFAST PULSE AMPLIFICATION

The Yb-doped alumina platform is well suited for pulse amplification, leveraging low material nonlinearity, large saturation energy, and long upper-state lifetime. The nonlinear index (n_2) of alumina is 4.8×10^{-20} m²/W [50], which is comparable to that of silica and approximately 5–10 times lower than that of silicon nitride [58]. Combined with the short amplifier length of 5.5 cm, this minimizes the nonlinear phase accumulation. Additionally, we calculated a large saturation energy of 730 nJ (see Supplementary Information), such that each pulse depletes only a small fraction of the population inversion and therefore experiences nearly constant gain throughout the pulse, ensuring negligible distortion and gain depletion.

These favorable properties enable low-distortion, energetic ultrafast pulse amplification of a Yb-fiber mode-locked laser emitting at a center wavelength of 1050 nm. The initial 125 fs pulses were first pre-chirped to 5.2 ps in normally dispersive HI 1060 fiber to reduce the peak power and mitigate nonlinear optical effects [59], then amplified in the integrated Yb amplifier, and finally re-compressed using a grating compressor (Fig. 3a). The input and output optical spectra are shown in Fig. 3b and the average power was measured using a calibrated optical spectrum analyzer (OSA). For low-energy input pulses of 1.8 pJ, we measured a net gain of 18.9 dB (Fig. 3c). This value is lower than the small-signal gain for CW amplification, because the pulse spectrum is not centered within the amplifier’s peak gain band of 1010–1030 nm (Fig. 2b). Increasing the input pulse energy to 100 pJ yields record-high output pulse energies of 5.3 nJ (Fig. 3d). At output energies above 1 nJ, however, the compressed pulse duration begins to broaden, increasing from 200 fs to 370 fs (Fig. 3e), due to nonlinear chirp accumulated in the amplifier that cannot be compensated by the grating compressor [60]. A maximum peak power

of 14 kW after compression is achieved at an output pulse energy of 4.4 nJ, due to the narrower pulse width. Given the long upper-state lifetime of 250 μ s, reducing the pulse repetition rate could further increase the output pulse energy. In practice, however, the achievable pulse energy may be limited by nonlinear distortions, as observed here. These distortions can be further mitigated by increasing the mode area or by balancing dispersion, gain, and nonlinearity to approach a self-similar pulse-evolution regime [61].

V. SUPERCONTINUUM GENERATION

After amplification in the Yb-doped alumina amplifier, femtosecond pulses with energies of 2.6 nJ (measured in fiber) were injected into silicon nitride (Si₃N₄) and silica-tantala (SiO₂:Ta₂O₅) supercontinuum waveguides [46, 62, 63] (Fig. 4a(3.1) and 4a(3.2)). The silicon nitride waveguide, measuring 700 nm in thickness, 900 nm in width, and 50 mm in length, was designed to exhibit anomalous dispersion at 1050 nm and to generate a visible dispersive wave near 765 nm (integrated dispersion in Supplementary Information). This dispersion enables a supercontinuum spectrum spanning approximately 600 to 1700 nm at a loaded pulse energy of 610 pJ (Fig. 4b).

Repetition-rate beatnotes measured across the spectrum confirm that the supercontinuum remains coherent over the full bandwidth (Fig. 4b). For silica-tantala waveguides, the material dispersion was optimized by varying the material composition [64], while the geometric dispersion was tuned by sweeping waveguide widths from 550 to 950 nm. At loaded pulse energies of 1.1 nJ, these waveguides generate supercontinua with dispersive wave locations spanning from red to the blue (Fig. 4a(3.3) and Fig. 4c).

Notably, the green line at 538 nm is well-suited for f-2f locking, enabling stabilized frequency combs [65].

In this experiment, we used discrete Yb-doped amplifier and supercontinuum waveguide chips together with fiber-based WDMs and isolators. In a fully integrated system, the WDMs can be implemented on chip, and the isolator can be eliminated when the Yb-doped amplifier is heterogeneously integrated with the nonlinear photonic circuit. Bidirectional pumping can be implemented via additional pump-injection waveguides with on-chip WDMs or directly through the nonlinear photonic waveguide.

VI. DISCUSSION AND OUTLOOK

We have demonstrated an integrated Yb-doped gain platform with a small-signal gain of 28.6 dB, greater than 0.5 W output power, and an optical-to-optical efficiency over 70%. The broad gain bandwidth (1010–1090 nm), together with the low nonlinearity, long lifetime, and

large saturation energy, enables pulsed amplification to record-high pulse energies of 5.3 nJ and compressed peak powers of 14 kW. The high pulse energies drive integrated supercontinuum generation spanning from the NIR deep into the blue wavelengths.

Direct f-2f locking becomes feasible when combined with heterogeneously integrated thin film lithium niobate [46] or effective $\chi^{(2)}$ processes in silicon nitride [66–68]. Looking forward, full integration of a pulse generator can be realized on the Yb-gain platform established in this work via a Mamyshev oscillator [9, 69], a passive Kerr soliton cavity [70], an electro-optic modulator [8], or a saturable absorber for mode locking [71, 72]. Furthermore, dispersion engineering enables pulse pre-chirping – in both anomalous and normal regimes – within nanophotonic waveguides, offering a direct on-chip integration of the free-space compressor utilized in this study. This line of development establishes a foundational architecture for optical frequency synthesizers [73], optical clocks [11], and microwave oscillators [12, 13] operating directly in the visible-NIR regime.

Beyond the visible-NIR ultrafast photonics, this platform also provides a highly scalable architecture for producing multi-output, multi-watt CW light near 1 μm via an amplifier array [74] seeded by a single laser. When integrated with beam emitter arrays, this capability promises to enable scalable optical tweezer arrays for Cs [4], along with other quantum computing applications. Furthermore, it establishes a foundation for nonlinear frequency conversion capable of providing the critical visible and ultraviolet cooling lasers required for ultracold atoms, ions, and molecules [3, 10, 16]. Finally, the co-sputtering approach demonstrated here is not restricted to specific host materials or dopants. For instance, co-doping Er with Yb can significantly increase the pump absorption efficiency [27, 75], enhancing the suitability for high-power amplification in the telecommunication band, pushing performance beyond currently existing limits.

ACKNOWLEDGMENTS

Major funding for this work is provided by the DARPA (D23AP00251-00), along with supports from

the Office of the Under Secretary of Defense for Research and Engineering (FA8721-05-C-0002), and Harvard University. S.A.D. acknowledges support from AFOSR (FA9550-22-1-0483) and NSF (OMA-2016244). T.Z. acknowledges postdoctoral fellowship support from the Gordon and Betty Moore Foundation.

The alumina and silicon nitride devices were fabricated in the Harvard Center for Nanoscale Systems and MIT.nano cleanrooms. We thank J. Deng and E. Macomber for helpful discussions. We acknowledge Martin Chicoine (Laboratoire René-J-A-Lévesque, Université de Montréal) for conducting the Rutherford backscattering spectrometry measurements. We thank T. P. Letsou, F. Capasso, X. Fan, G. Semeghini, J. Doyle (Harvard), P. Delfyett (CREOL), W. Loh, D. Gray (MIT Lincoln Laboratory), M. Tran, T. Komljenovic (Nexus Photonics), Y. Wan (KAUST), and K. Van Gasse (Ghent) for discussions and/or internal review. K.Y. acknowledges discussions with J. Cohen (DARPA) and M. Lipson (Columbia).

Any subjective opinions, interpretations, conclusions that might be expressed in the paper do not necessarily represent the views of the US Government.

Data availability The data that support the plots within this paper and other findings of this study are available from the corresponding author upon reasonable request.

Code availability The code used to produce the plots within this paper is available from the corresponding author upon reasonable request.

Conflict of interest P.C., N.B. and T.-H.W. are affiliated with Chi3 Optics, which develops fiber lasers and integrated frequency comb systems. D.R.C. and Z.L.N. are affiliated with, and hold an ownership interest in, Octave Photonics, which manufactures and provides nanophotonic devices and services.

-
- [1] Desurvire, E., Simpson, J. R. & Becker, P. High-gain erbium-doped traveling-wave fiber amplifier. *Optics Letters* **12**, 888–890 (1987).
 - [2] Hanna, D. *et al.* Continuous-wave oscillation of a monomode ytterbium-doped fibre laser. *Electronics Letters* **24**, 1111–1113 (1988).
 - [3] Anderegg, L. *et al.* An optical tweezer array of ultracold molecules. *Science* **365**, 1156–1158 (2019).
 - [4] Manetsch, H. J. *et al.* A tweezer array with 6,100 highly coherent atomic qubits. *Nature* **647**, 60–67 (2025).
 - [5] Steinmetz, T. *et al.* Laser frequency combs for astronomical observations. *Science* **321**, 1335–1337 (2008).
 - [6] Carlson, D. R. *et al.* Ultrafast electro-optic light with subcycle control. *Science* **361**, 1358–1363 (2018).
 - [7] Lesko, D. M. *et al.* A six-octave optical frequency comb from a scalable few-cycle erbium fibre laser. *Nature Photonics* **15**, 281–286 (2021).
 - [8] Guo, Q. *et al.* Ultrafast mode-locked laser in nanophotonic lithium niobate. *Science* **382**, 708–713

- (2023).
- [9] Qiu, Z. *et al.* High-pulse-energy integrated mode-locked lasers based on a Mamyshev oscillator. *arXiv preprint arXiv:2509.05133* (2025).
 - [10] Ludlow, A. D., Boyd, M. M., Ye, J., Peik, E. & Schmidt, P. O. Optical atomic clocks. *Reviews of Modern Physics* **87**, 637–701 (2015).
 - [11] Newman, Z. L. *et al.* Architecture for the photonic integration of an optical atomic clock. *Optica* **6**, 680–685 (2019).
 - [12] Kudelin, I. *et al.* Photonic chip-based low-noise microwave oscillator. *Nature* **627**, 534–539 (2024).
 - [13] Nakamura, T. *et al.* Low-noise microwaves from free-running frequency combs and electrical feed-forward phase noise compensation. *Nature Photonics* 1–6 (2026).
 - [14] Paschotta, R., Nilsson, J., Tropper, A. C. & Hanna, D. C. Ytterbium-doped fiber amplifiers. *IEEE Journal of Quantum Electronics* **33**, 1049–1056 (1997).
 - [15] Chiu, N.-C. *et al.* Continuous operation of a coherent 3,000-qubit system. *Nature* **646**, 1075–1080 (2025).
 - [16] Vilas, N. B. *et al.* An optical tweezer array of ultracold polyatomic molecules. *Nature* **628**, 282–286 (2024).
 - [17] Xu, C., Nedergaard, M., Fowell, D. J., Friedl, P. & Ji, N. Multiphoton fluorescence microscopy for in vivo imaging. *Cell* **187**, 4458–4487 (2024).
 - [18] Wilken, T. *et al.* A spectrograph for exoplanet observations calibrated at the centimetre-per-second level. *Nature* **485**, 611–614 (2012).
 - [19] Metcalf, A. J. *et al.* Stellar spectroscopy in the near-infrared with a laser frequency comb. *Optica* **6**, 233–239 (2019).
 - [20] Van den Hoven, G. *et al.* Photoluminescence characterization of Er-implanted Al₂O₃ films. *Applied Physics Letters* **62**, 3065–3067 (1993).
 - [21] Fleuster, M., Buchal, C., Snoeks, E. & Polman, A. Rapid thermal annealing of MeV erbium implanted LiNbO₃ single crystals for optical doping. *Applied Physics Letters* **65**, 225–227 (1994).
 - [22] Min, B. *et al.* Erbium-implanted high-Q silica toroidal microcavity laser on a silicon chip. *Physical Review A-Atomic, Molecular, and Optical Physics* **70**, 033803 (2004).
 - [23] Bradley, J., Ay, F., Wörhoff, K. & Pollnau, M. Fabrication of low-loss channel waveguides in Al₂O₃ and Y₂O₃ layers by inductively coupled plasma reactive ion etching. *Applied Physics B* **89**, 311–318 (2007).
 - [24] Bradley, J. D. *et al.* Monolithic erbium-and ytterbium-doped microring lasers on silicon chips. *Optics Express* **22**, 12226–12237 (2014).
 - [25] Belt, M. & Blumenthal, D. J. Erbium-doped waveguide DBR and DFB laser arrays integrated within an ultra-low-loss Si₃N₄ platform. *Optics Express* **22**, 10655–10660 (2014).
 - [26] Aghajani, A., Murugan, G. S., Sessions, N., Apostolopoulos, V. & Wilkinson, J. Waveguide lasers in ytterbium-doped tantalum pentoxide on silicon. *Optics Letters* **40**, 2549–2552 (2015).
 - [27] Bonneville, D. B., Frankis, H. C., Wang, R. & Bradley, J. D. Erbium-ytterbium co-doped aluminium oxide waveguide amplifiers fabricated by reactive co-sputtering and wet chemical etching. *Optics Express* **28**, 30130–30140 (2020).
 - [28] Frankis, H. C. *et al.* Erbium-doped TeO₂-coated Si₃N₄ waveguide amplifiers with 5 dB net gain. *Photonics Research* **8**, 127–134 (2020).
 - [29] Liu, Y. *et al.* A photonic integrated circuit-based erbium-doped amplifier. *Science* **376**, 1309–1313 (2022).
 - [30] Singh, N. *et al.* Watt-class silicon photonics-based optical high-power amplifier. *Nature Photonics* **19**, 307–314 (2025).
 - [31] Jongbloed, B., Osornio-Martinez, C., Wang, K., Dijkstra, M. & García-Blanco, S. Fiber-to-fiber gain in Nd-doped aluminium oxide waveguide amplifiers. *Optics Express* **34**, 4522–4534 (2026).
 - [32] Osornio-Martinez, C., Bonneville, D., Dijkstra, M., do Nascimento Jr, A. & Garcia-Blanco, S. Broadband packaged erbium-doped polycrystalline Al₂O₃ waveguide amplifier with 24 dB external net gain. *Optics Express* **33**, 28985–28994 (2025).
 - [33] Niffenegger, R. J. *et al.* Integrated multi-wavelength control of an ion qubit. *Nature* **586**, 538–542 (2020).
 - [34] Tran, M. A. *et al.* Extending the spectrum of fully integrated photonics to submicrometre wavelengths. *Nature* **610**, 54–60 (2022).
 - [35] Renaud, D. *et al.* Sub-1 Volt and high-bandwidth visible to near-infrared electro-optic modulators. *Nature Communications* **14**, 1496 (2023).
 - [36] Chen, H.-J. *et al.* Towards fibre-like loss for photonic integration from violet to near-infrared. *Nature* **649**, 338–344 (2026).
 - [37] Huang, G. *et al.* Thermorefractive noise in silicon-nitride microresonators. *Physical Review A* **99**, 061801 (2019).
 - [38] Panuski, C., Englund, D. & Hamerly, R. Fundamental thermal noise limits for optical microcavities. *Physical Review X* **10**, 041046 (2020).
 - [39] Stern, L. *et al.* Ultra-precise optical-frequency stabilization with heterogeneous III-V/Si lasers. *Optics Letters* **45**, 5275–5278 (2020).
 - [40] Dacha, S. K. *et al.* Frequency-stable nanophotonic microcavities via integrated thermometry. *Nature Photonics* **20**, 71–78 (2026).
 - [41] Torab Ahmadi, P. *et al.* Low-loss and low-temperature Al₂O₃ thin films for integrated photonics and optical coatings. *Journal of Vacuum Science & Technology A* **42** (2024).
 - [42] Kang, Y. *et al.* Monolithic germanium/silicon avalanche photodiodes with 340 GHz gain-bandwidth product. *Nature Photonics* **3**, 59–63 (2009).
 - [43] Sun, C. *et al.* Single-chip microprocessor that communicates directly using light. *Nature* **528**, 534–538 (2015).
 - [44] Atabaki, A. H. *et al.* Integrating photonics with silicon nanoelectronics for the next generation of systems on a chip. *Nature* **556**, 349–354 (2018).
 - [45] Churaev, M. *et al.* A heterogeneously integrated lithium niobate-on-silicon nitride photonic platform. *Nature Communications* **14**, 3499 (2023).
 - [46] Brodnik, G. M. *et al.* Monolithic 3D integration of tantalum pentoxide nonlinear photonics. *Nature* (2026).
 - [47] Browaeys, A. & Lahaye, T. Many-body physics with individually controlled Rydberg atoms. *Nature Physics* **16**, 132–142 (2020).
 - [48] Wu, K. *et al.* Vernier microcombs for integrated optical atomic clocks. *Nature Photonics* **19**, 400–406 (2025).
 - [49] DeSalvo, R., Said, A. A., Hagan, D. J., Van Stryland, E. W. & Sheik-Bahae, M. Infrared to ultraviolet measurements of two-photon absorption and n_2 in wide bandgap solids. *IEEE Journal of Quantum Electronics*

- 32**, 1324–1333 (1996).
- [50] Dragic, P., Cavillon, M. & Ballato, J. The linear and nonlinear refractive index of amorphous Al_2O_3 deduced from aluminosilicate optical fibers. *International Journal of Applied Glass Science* **9**, 421–427 (2018).
- [51] Kip, D. Photorefractive waveguides in oxide crystals: fabrication, properties, and applications. *Applied Physics B: Lasers & Optics* **67** (1998).
- [52] Jones, J. *et al.* Channel waveguide laser at 1 μm in Yb-indiffused LiNbO_3 . *Optics Letters* **20**, 1477–1479 (1995).
- [53] Zeng, T. *et al.* Injection locking of integrated erbium-based laser. *CLEO: Applications and Technology* (2025).
- [54] Mu, J. *et al.* Monolithic integration of Al_2O_3 and Si_3N_4 toward double-layer active–passive platform. *IEEE Journal of Selected Topics in Quantum Electronics* **25**, 1–11 (2019).
- [55] Paschotta, R. *et al.* Lifetime quenching in Yb-doped fibres. *Optics Communications* **136**, 375–378 (1997).
- [56] Loiko, P. *et al.* Quantitative analysis of cooperative upconversion in Al_2O_3 : Yb^{3+} . *Optical Materials* **162**, 116798 (2025).
- [57] Purnawirman *et al.* C- and L-band erbium-doped waveguide lasers with wafer-scale silicon nitride cavities. *Optics Letters* **38**, 1760–1762 (2013).
- [58] Gao, M. *et al.* Probing material absorption and optical nonlinearity of integrated photonic materials. *Nature Communications* **13**, 3323 (2022).
- [59] Strickland, D. & Mourou, G. Compression of amplified chirped optical pulses. *Optics Communications* **55**, 447–449 (1985).
- [60] Agrawal, G. P. Nonlinear Fiber Optics. In *Nonlinear Science at the Dawn of the 21st Century*, 195–211 (Springer, 2000).
- [61] Fermann, M. E., Kruglov, V., Thomsen, B., Dudley, J. M. & Harvey, J. D. Self-similar propagation and amplification of parabolic pulses in optical fibers. *Physical Review Letters* **84**, 6010 (2000).
- [62] Lamee, K. F., Carlson, D. R., Newman, Z. L., Yu, S.-P. & Papp, S. B. Nanophotonic tantalum waveguides for supercontinuum generation pumped at 1560 nm. *Optics Letters* **45**, 4192–4195 (2020).
- [63] Jung, H. *et al.* Tantalum Kerr nonlinear integrated photonics. *Optica* **8**, 811–817 (2021).
- [64] Carollo, A. R. *et al.* Amorphous metal oxide mixtures for high-Q integrated nonlinear photonics. *arXiv preprint arXiv:2508.14887* (2025).
- [65] Oh, D. Y. *et al.* Coherent ultra-violet to near-infrared generation in silica ridge waveguides. *Nature Communications* **8**, 13922 (2017).
- [66] Lu, X., Moille, G., Rao, A., Westly, D. A. & Srinivasan, K. Efficient photoinduced second-harmonic generation in silicon nitride photonics. *Nature Photonics* **15**, 131–136 (2021).
- [67] Nitiss, E., Hu, J., Stroganov, A. & Brès, C.-S. Optically reconfigurable quasi-phase-matching in silicon nitride microresonators. *Nature Photonics* **16**, 134–141 (2022).
- [68] Yuan, Z. *et al.* Efficient and wavelength-tunable second-harmonic generation toward the green gap. *Science Advances* **11**, eadw2781 (2025).
- [69] Liu, Z., Ziegler, Z. M., Wright, L. G. & Wise, F. W. Megawatt peak power from a Mamyshev oscillator. *Optica* **4**, 649–654 (2017).
- [70] Herr, T. *et al.* Temporal solitons in optical microresonators. *Nature Photonics* **8**, 145–152 (2014).
- [71] Keller, U. *et al.* Semiconductor saturable absorber mirrors (SESAMs) for femtosecond to nanosecond pulse generation in solid-state lasers. *IEEE Journal of Selected Topics in Quantum Electronics* **2**, 435–453 (1996).
- [72] Byun, H. *et al.* Integrated low-jitter 400-MHz femtosecond waveguide laser. *IEEE Photonics Technology Letters* **21**, 763–765 (2009).
- [73] Spencer, D. T. *et al.* An optical-frequency synthesizer using integrated photonics. *Nature* **557**, 81–85 (2018).
- [74] Qiu, Z. *et al.* Hybrid integrated multi-lane erbium-doped Si_3N_4 waveguide amplifiers. *European Conference on Optical Communication* 1721–1724 (2024).
- [75] Strohhofer, C. & Polman, A. Absorption and emission spectroscopy in Er^{3+} - Yb^{3+} doped aluminum oxide waveguides. *Optical Materials* **21**, 705–712 (2003).

Supplementary Information for: Integrated ytterbium gain for visible-near-infrared photonics

Tianyi Zeng^{1,†}, Erik W. Masselink^{1,2,†}, Tsung-Han Wu^{3,4}, Nathan Brooks⁴, Peter Chang⁴, Grisha Spektor⁵, Zachary L. Newman⁵, Danxian Liu¹, Scott B. Papp^{6,7}, David R. Carlson⁵, Scott A. Diddams^{3,7}, Kiyoul Yang^{1,*}

¹John A. Paulson School of Engineering and Applied Sciences, Harvard University

²Department of Electrical Engineering and Computer Science, Massachusetts Institute of Technology

³Electrical, Computer and Energy Engineering, University of Colorado Boulder

⁴Chi3 Optics LLC, Boulder, CO, USA

⁵Octave Photonics, Louisville, CO, USA

⁶Time and Frequency Division, National Institute of Standards and Technology, Boulder, CO, USA

⁷Department of Physics, University of Colorado Boulder

[†]These authors contributed equally to this work.

*kiyoul@seas.harvard.edu

Contents

S1. Methods		11
S1.1. Numerical modeling		11
S1.2. Fabrication		13
S1.3. CW amplification		14
S1.4. Ultrafast pulse amplification		14
S1.5. Supercontinuum generation		15
S2. Additional information		16
S2.1. Passive loss characterization of ytterbium-doped alumina waveguides		16
S2.2. Rutherford backscattering spectrometry		17
S2.3. Photoluminescence lifetime measurement		18
S2.4. DFB laser characterization		19
S2.5. Optical gain and noise figure measurement		19
S2.6. Device performance comparison		20
Supplementary References		23

S1. Methods

S1.1. Numerical modeling



FIG. S1. **Yb gain modeling.** (a) Yb^{3+} energy diagram in an alumina host [SI1]. (b) Picture of the Yb amplifier showing green luminescence quenching.

The ytterbium-doped gain medium is modeled as an effective two-level system consisting of the ${}^2F_{7/2}$ ground-state manifold and the ${}^2F_{5/2}$ excited-state manifold (Fig. S1a). The ground-state manifold is denoted as level 1 and the metastable upper level manifold as level 2. We pump at 976 nm, corresponding to the lowest Stark levels of the ${}^2F_{5/2}$ manifold, because this wavelength provides a large absorption cross section and a relatively small quantum defect compared with shorter-wavelength Yb pump bands. Although Yb has been demonstrated to be predominantly inhomogeneously broadened in Al-doped silica [SI2] and is therefore likely also inhomogeneously broadened in the alumina host, we treat the ions as a single effective species described by ensemble-averaged cross sections, which is appropriate when operating at a single wavelength.

The population dynamics are governed by

$$\begin{aligned} \frac{dN_2}{dt} &= R_{12}N_1 - R_{21}N_2 - A_{21}N_2 - 2C_{\text{ETU}}N_2^2, \\ \frac{dN_1}{dt} &= -R_{12}N_1 + R_{21}N_2 + A_{21}N_2 + 2C_{\text{ETU}}N_2^2, \\ N_1 + N_2 &= N_{\text{Yb}}, \end{aligned} \quad (\text{S1})$$

where N_i is the population density of level i and N_{Yb} is the average Yb concentration in the film measured with RBS (see Sec. S2.2). The spontaneous decay rate is given by $A_{21} = 1/\tau$ (see Sec. S2.3), and the stimulated transition rates are the sum of the stimulated emission rates from each frequency, written as

$$\begin{aligned} R_{ij} &= \sum_k R_{ij,k}, \\ R_{ij,k} &= \sigma_{ij,k} \phi_k = \frac{\sigma_{ij,k} P_k}{A_{\text{eff},k} h \nu_k}, \end{aligned} \quad (\text{S2})$$

where σ_{ij} is the absorption or emission cross section, ϕ is the photon flux density, h is the Planck constant, and ν_k is the frequency [SI3]. The effective mode area $A_{\text{eff},k}$ at the pump and signal frequencies was determined to be $1.85 \mu\text{m}^2$ and $1.90 \mu\text{m}^2$, respectively.

In contrast to rare-earth ions such as erbium or thulium, isolated Yb^{3+} does not possess higher-lying excited manifolds that strongly contribute to parasitic quenching. At high doping concentrations, however, Yb ion pairs and possible Er contamination can introduce additional loss channels, including energy-transfer upconversion (ETU) and potentially excited-state absorption (ESA), by enabling access to higher-energy states [SI1]. The resulting green emission is seen in Fig. S1b. In the present model, these effects are represented phenomenologically by a single homogeneous ETU coefficient, C_{ETU} , which was fit to the amplifier data to be $5 \times 10^{-18} \text{ cm}^3/\text{s}$. Alternatively, separating the Yb population into paired and unpaired species with different ETU coefficients or including excited-state absorption, produces similarly good agreement.

The evolution of the pump, signal, and amplified spontaneous emission (ASE) powers along the waveguide is

described by

$$\begin{aligned}
\frac{dP_s(z)}{dz} &= \Gamma_s [\sigma_{21,s}N_2(z) - \sigma_{12,s}N_1(z)] P_s(z) - \alpha_{0,s}P_s(z), \\
\frac{dP_{p,f}(z)}{dz} &= \Gamma_p [\sigma_{21,p}N_2(z) - \sigma_{12,p}N_1(z)] P_{p,f}(z) - \alpha_{0,p}P_{p,f}(z), \\
\frac{dP_{p,b}(z)}{dz} &= -\Gamma_p [\sigma_{21,p}N_2(z) - \sigma_{12,p}N_1(z)] P_{p,b}(z) + \alpha_{0,p}P_{p,b}(z), \\
\frac{dP_{\text{ASE},f}(z)}{dz} &= \Gamma_{\text{ASE}} [\sigma_{21,\text{ASE}}N_2(z) - \sigma_{12,\text{ASE}}N_1(z)] P_{\text{ASE},f}(z) \\
&\quad + \Gamma_{\text{ASE}} P_{\text{ASE}}^0 \sigma_{21,\text{ASE}} N_2(z) - \alpha_{0,\text{ASE}} P_{\text{ASE},f}(z), \\
\frac{dP_{\text{ASE},b}(z)}{dz} &= -\Gamma_{\text{ASE}} [\sigma_{21,\text{ASE}}N_2(z) - \sigma_{12,\text{ASE}}N_1(z)] P_{\text{ASE},b}(z) \\
&\quad - \Gamma_{\text{ASE}} P_{\text{ASE}}^0 \sigma_{21,\text{ASE}} N_2(z) + \alpha_{0,\text{ASE}} P_{\text{ASE},b}(z),
\end{aligned} \tag{S3}$$

where P_s , P_p , and P_{ASE} denote the signal, pump, and ASE powers, respectively, and the subscripts f and b denote forward- and backward-propagating waves. The doped region overlap factors $\Gamma_s = \Gamma_{\text{ASE}} = 89.5\%$ and $\Gamma_p = 90.2\%$ account for the spatial overlap of the optical mode in the doped region and are defined as $\Gamma_{s/p} = (\int_{\text{active}} I_{s/p} dA) / (\int_{\infty} I_{s/p} dA)$ [SI4]. The signal and pump modes are strongly co-located, with a calculated mutual overlap of 97.7%. The mode intensities were calculated using a finite element mode solver (Tidy3D). Approximating the full transverse distributions by power-independent overlap factors is less accurate near threshold, but becomes accurate in the high-pump, unsaturated-gain regime [SI5]. The passive propagation loss is denoted as α_0 (see Sec. S2.1).

Spontaneous emission contributes locally to the ASE power through the source term

$$P_{\text{ASE}}^0 = 2h\nu_{\text{ASE}}B, \tag{S4}$$

where h is Planck's constant, ν_{ASE} is the ASE center frequency, and B is the effective optical bandwidth [SI5]. In this model, ASE is treated as a single-frequency channel, where the bandwidth $B \approx 14$ THz is used to represent the main Yb gain bandwidth from 1010–1060 nm. The coupled propagation equations were solved self-consistently with boundary conditions given by the input signal and bidirectional pump powers, with $P_s(0) = P_{s,\text{in}}$, $P_{p,f}(0) = P_{p,f,\text{in}}$, $P_{p,b}(L) = P_{p,b,\text{in}}$, $P_{\text{ASE},f}(0) = 0$, and $P_{\text{ASE},b}(L) = 0$.

The signal absorption cross section was extracted from measurements of the small-signal loss in a 55-mm-long waveguide, whereas the pump absorption cross section was extracted from a 6.6-mm-long waveguide because of the stronger pump absorption. The Yb-related contribution to the loss was obtained by subtracting the coupling and passive waveguide losses from the measured small-signal loss, converted to the cross section using

$$\sigma_{12} = \frac{\alpha_{\text{active}}}{\Gamma N_{\text{Yb}}}, \tag{S5}$$

where α_{active} is the active absorption. At 976 nm, the emission and absorption cross sections were assumed to be equal, since previous work in Yb-doped alumina has shown that this wavelength is near the McCumber zero-line energy [SI6]. Finally, the signal emission cross section was extracted from the measured saturated active gain of 6.2 dB/cm in a 6.6-mm-long waveguide. The gain is defined as

$$g = \Gamma_s [\sigma_{21,s}N_2(z) - \sigma_{12,s}N_1(z)] \tag{S6}$$

and since $N_1 = N_2 = N_{\text{Yb}}/2$ at 50% inversion, in the small-signal and high-pump regime, we obtain

$$\sigma_{21,s} = \sigma_{12,s} + \frac{2g}{\Gamma_s N_{\text{Yb}}}. \tag{S7}$$

The resulting cross sections are $\sigma_{12,p} = 1.9 \times 10^{-20}$ cm², $\sigma_{21,p} = 1.9 \times 10^{-20}$ cm², $\sigma_{12,s} = 3.0 \times 10^{-22}$ cm², and $\sigma_{21,s} = 5.2 \times 10^{-21}$ cm². We can then calculate the saturation energy as $E_{\text{sat}} = \frac{h\nu A_{\text{eff}}}{\Gamma_s (\sigma_{21,s} + \sigma_{12,s})} = 730$ nJ and the saturation power as $P_{\text{sat},W} = \frac{E_{\text{sat}}}{\tau_{21}} = 2.9$ mW.

S1.2. Fabrication

The fabrication process of the ytterbium-doped AlO_x photonic circuits started from the growth of the gain film (Fig. S2). We used an RF magnetron co-sputtering technique [SI7–SI9] to deposit a $1.08\text{-}\mu\text{m}$ $\text{Yb}:\text{AlO}_x$ film on top of a $4\text{-}\mu\text{m}$ wet thermal oxide layer, which served as the bottom cladding. The surface roughness of the sputtered film was measured by atomic force microscopy (AFM, Jupiter XR) to be 120 pm (Fig. S3a-b). The thickness and refractive index of the $\text{Yb}:\text{AlO}_x$ film were characterized by SEM and ellipsometry (Woollam), yielding a thickness of 1080 nm and a refractive index of 1.66 at 1030 nm (Fig. S3c).

Nanophotonic structures were then patterned with electron-beam lithography (Elionix) on a negative resist (ma-N 2400 series) followed by a Cl-based reactive ion etching (RIE) process [SI10]. The etch pressure was carefully tuned to produce smooth sidewalls with a sidewall angle of 52° and a controllable lateral etch of $500\text{--}800\text{ nm}$ on each side of the waveguide. For waveguide patterns narrower than the total lateral etch offset, the etched structure evolves into a triangular cross section, with both height and width decreasing as the etch proceeds. Using this technique, we engineered a three-dimensional inverse taper at the amplifier facet (see Fig. 1 and Fig. S4) to minimize facet reflection and insertion loss.

Following the patterning of the active region, $5\text{ }\mu\text{m}$ of SiO_2 was deposited as the top cladding. Finally, we annealed the devices at $725\text{ }^\circ\text{C}$ for 4 hours to reduce the amount of hydrogen bonds in the PECVD oxide [SI11]. The dies were then diced and polished for measurement.

The supercontinuum waveguides were fabricated in a similar fashion. Silicon nitride (SiN) was grown by low-pressure chemical vapor deposition (LPCVD) on a $4\text{-}\mu\text{m}$ wet thermal oxide layer. Waveguides were patterned in the same manner as described above, except that the RIE was performed using F-based chemistry. The SiN waveguides were annealed at $1050\text{ }^\circ\text{C}$ for 8 hours after etching. We then deposited $2\text{ }\mu\text{m}$ of silicon oxide as the top cladding using LPCVD. Finally, we annealed the device again at $1050\text{ }^\circ\text{C}$ for 8 hours.

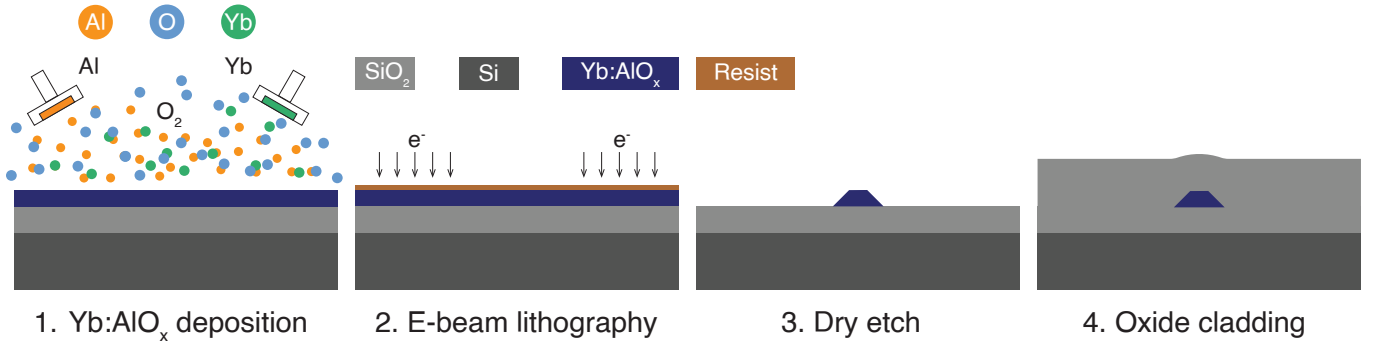


FIG. S2. $\text{Yb}:\text{AlO}_x$ photonic chip fabrication flow.

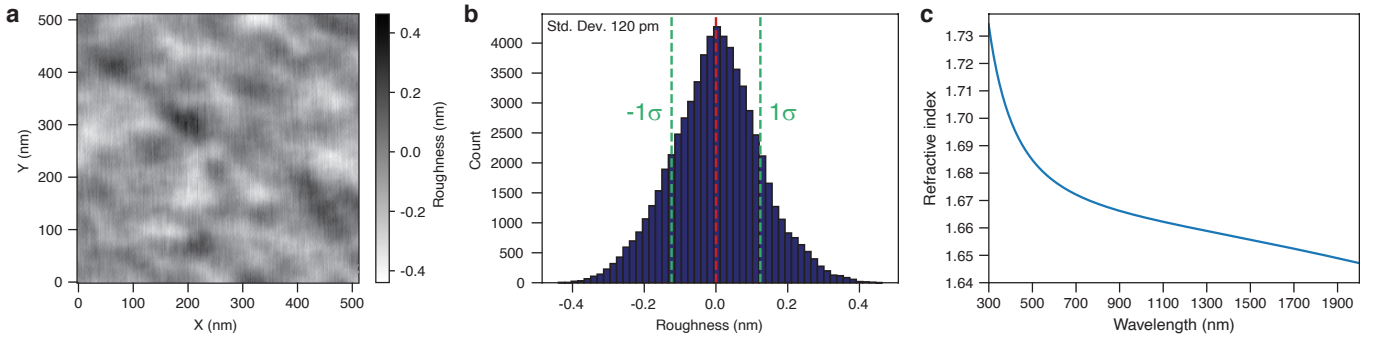


FIG. S3. **Sputtered $\text{Yb}:\text{AlO}_x$ film characteristics.** (a) Surface roughness measured by AFM. (b) Histogram of the AFM data showing a standard deviation of 120 pm . (c) Refractive index of the $\text{Yb}:\text{AlO}_x$ thin film.

S1.3. CW amplification

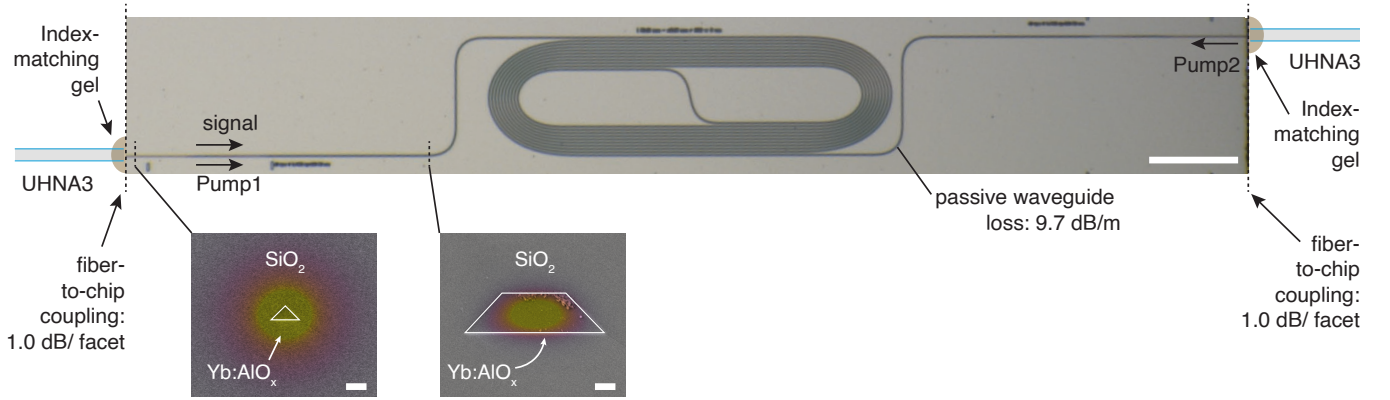


FIG. S4. **Input and output fiber-coupled integrated Yb-doped amplifier.** The amplifier chip facets were polished close to normal to the input and output waveguide direction. The waveguides are tapered in both width and height to facilitate efficient coupling and low back-reflection. Cleaved UHNA3 fibers were butt-coupled to the waveguide alongside index-matching gel. SEM images of the waveguide cross-sections (also presented in Fig. 1 in the main text) are included for reference. The measured fiber-to-chip coupling loss and passive waveguide transmission losses are approximately 1.0 dB per facet and 9.7 dB per meter, respectively.

The amplifier was pumped bidirectionally using two 976 nm diode lasers (Thorlabs BL976-PAG900). The signal was provided by a tunable CW laser covering 1010–1100 nm (Toptica CTL). Two 980/1060 nm wavelength-division multiplexers (WDMs, Thorlabs WD9860AB) were used to combine the pump and signal at the input and to separate them at the output. Ultra-high-numerical-aperture fiber (Nufern/Coherent UHNA3) with a mode-field diameter of 2.6 μm at 1100 nm [SI12] was used for chip coupling (Fig. S4). All other fiber segments were HI 1060.

Input and output spectra were recorded with an optical spectrum analyzer (Yokogawa AQ6370D, 600–1700 nm) at a resolution bandwidth of 0.1 nm. The OSA was calibrated using an integrating-sphere power sensor (Thorlabs S145C). The calibrated measurements were then converted to off-chip and on-chip powers using the WDM and fiber-chip coupling loss. The optical gain was extracted by taking the difference between the peak output power and peak input power (Fig. S11).

S1.4. Ultrafast pulse amplification

The pulsed source used for the ultrafast pulse amplification is derived from an all-fiber Er-doped ultrafast frequency comb operating in the 1.55- μm spectral region. The oscillator generates stable femtosecond pulses that can be externally compressed to durations below 50 fs, enabling high peak power for efficient nonlinear conversion. These pulses are subsequently launched into a highly nonlinear fiber, where significant spectral broadening occurs via third-order nonlinear (χ^3) processes. In particular, dispersive wave generation facilitates efficient energy transfer from the soliton to the 1- μm spectral region. The generated 1- μm dispersive wave component is spectrally filtered and used as a coherent seed for a Yb-doped fiber amplifier. After amplification, a stable 1- μm frequency comb is obtained with an average output power exceeding 150 mW and compressed pulse duration below 150 fs, while fully preserving comb coherence and phase stability.

The pulsed optical gain measurement used the same pumping scheme as the CW gain measurement. A total of 4 m of HI 1060 fiber (including the fiber lengths constituting the polarization controller and the isolator) was inserted between the pulsed laser and the WDM to pre-stretch the pulse to a width of 5.2 ps. The same OSA resolution bandwidth of 0.1 nm was used for the measurement. The pulse power was calculated from the measured spectra by accounting for the wavelength-dependent WDM loss to obtain the correct off-chip power and the on-chip pulse power was then calculated by compensating for the chip coupling loss of 1.0 dB per facet.

After amplification, the pulses were compressed using an in-house pulse compressor consisting of two transmission gratings (Coherent LightSmyth), with a design wavelength of 1040 nm and a groove density of 1000 grooves/mm to provide anomalous dispersion. The output from the compressor was then sent to an autocorrelator (Femtochrome FR-103XL) for pulse width characterization.

S1.5. Supercontinuum generation

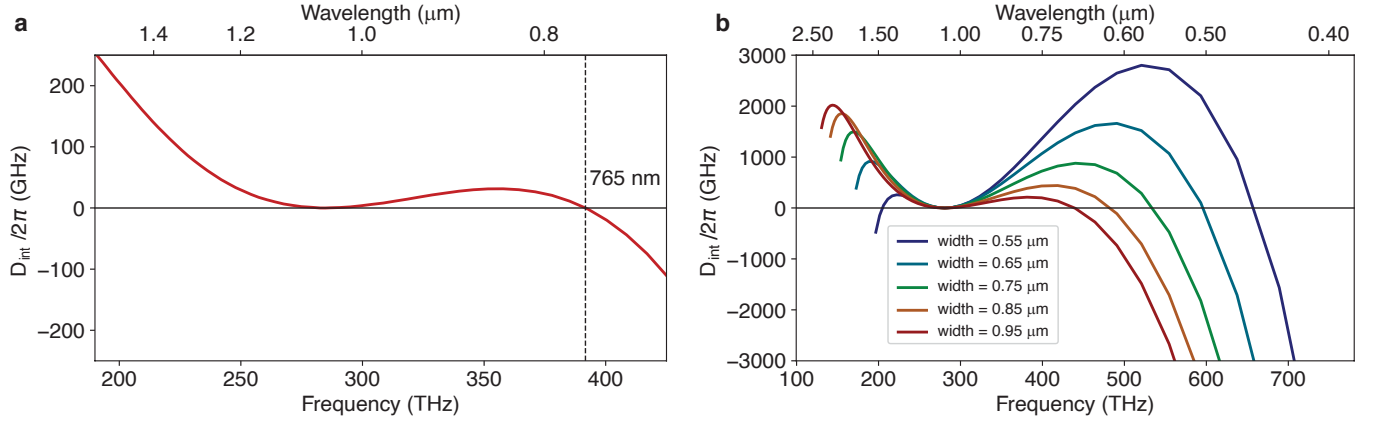


FIG. S5. **Integrated dispersion for supercontinuum waveguides.** (a) Integrated dispersion for the TE mode in the Si_3N_4 waveguides with a width of $0.9 \mu\text{m}$. (b) Integrated dispersion of the TE mode in the $\text{SiO}_2:\text{Ta}_2\text{O}_5$ waveguides with widths ranging from $0.55 \mu\text{m}$ to $0.95 \mu\text{m}$.

For the supercontinuum generation experiments, we adopted a pre-compression scheme to avoid compressor insertion loss. The remainder of the pulse amplification setup was identical to that described in section S1.4. Following amplification, the pulse was sent through an optical isolator to suppress reflections from the facets of the passive waveguides. Polarization was adjusted using a paddle-based fiber polarization controller, and lensed fibers were used for coupling into and out of the passive supercontinuum waveguides.

The output spectra were monitored using two OSAs to cover the wavelength range from 400 to 1800 nm: a short-wavelength OSA (350–1200 nm, Yokogawa AQ6373E) and a long-wavelength OSA (1200–2400 nm, Yokogawa AQ6375). In grating-based spectrum analyzers, shorter-wavelength light can overlap longer-wavelength signals through higher diffraction orders, producing spurious spectral features. The short-wavelength OSA suppresses these artifacts using built-in high order optical cut filters. Because the long-wavelength OSA does not include such filters, we inserted a long-pass filter with a cut-on wavelength of 1050 nm to block the short-wavelength components. To compensate for the filter loss, the 1200–2400 nm spectrum was scaled to match the 350–1200 nm spectrum at the 1200 nm overlap point.

We performed supercontinuum generation experiments in both Si_3N_4 and $\text{SiO}_2:\text{Ta}_2\text{O}_5$ waveguides. The Si_3N_4 waveguides were fabricated in-house with a waveguide height of 700 nm, a width of 900 nm, and oxide cladding to target a dispersive wave around 765 nm. The integrated dispersion for the TE mode is shown in Fig. S5a. The waveguide was 50 mm long and inverse-tapered at the facets to a width of 200 nm, improving the coupling efficiency to 6.3 dB/facet. The $\text{SiO}_2:\text{Ta}_2\text{O}_5$ waveguides with various waveguide widths were used to generate dispersive waves at visible wavelengths spanning from 476 to 644 nm [SI13, SI14]. To obtain the desired dispersion profile, the waveguides were air-clad and SiO_2 was added as a dopant [SI15] (Fig. S5b). Waveguide tapers were implemented to improve the coupling efficiency to 3.7 dB/facet for the $\text{SiO}_2:\text{Ta}_2\text{O}_5$ waveguides.

The phase coherence of the Si_3N_4 supercontinuum generation was evaluated by measuring the repetition rate beatnotes across the generated spectrum by using different combinations of optical bandpass filters and photodetectors. One photodetector covers the wavelength region of 900–1700 nm (Newport 1811-FC-AC, PD1), while the other covers a wavelength range of 320–1000 nm (Newport 1801-FC-AC, PD2). The two bandpass filters cover the wavelength ranges of 1045–1055 nm (Thorlabs FBH1050-10, BP1) and 778.5–781.5 nm (Thorlabs FBH780-3, BP2).

S2. Additional information

S2.1. Passive loss characterization of ytterbium-doped alumina waveguides

The passive insertion loss of the amplifier was measured at 1060 nm by using a YDFA to drive the device into gain saturation, thereby isolating the passive loss. A wavelength of 1060 nm was used instead of 1030 nm due to the operation bandwidth of the YDFA. To separate coupling loss from passive waveguide loss, we measured both 80-mm spiral amplifiers, 55-mm spiral amplifiers, and short 6.6-mm amplifiers. Because of yield limitations, the short devices could not be measured with the same 692-nm bottom taper width, so devices with 807-nm and 853-nm taper widths were characterized instead. These showed identical insertion losses of 2.1 dB. Given this close agreement, data from all taper widths were fit together, yielding an estimated coupling loss of 1.0 dB per facet and a passive waveguide loss of 9.7 dB/m (Fig. S6a). To validate this result, we also measured the quality factors of 100- μm -radius microring resonators from a subsequent fabrication batch at 1089.5 nm to avoid the Yb absorption at 1060 nm, which gave an inferred loss of 14.4 dB/m (Fig. S6b). The input power for the quality factor measurements was increased to just below the onset of the thermal bistability, so that the active loss was maximally saturated while avoiding thermally induced resonance shifts that would complicate quality factor extraction. The measured loss is higher than the cutback value, which we attribute to residual active loss and bending loss.

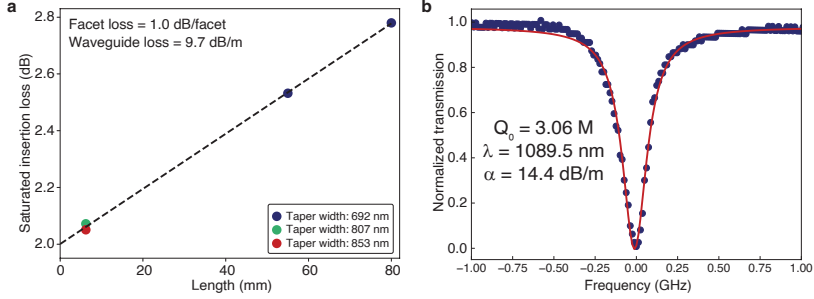


FIG. S6. **Passive insertion loss characterization.** (a) Cutback measurement for passive waveguide loss and coupling loss extraction. (b) Microring resonator quality factor measurement to extract the passive waveguide loss. Q_0 , fitted intrinsic quality factor; λ , center wavelength; α , inferred propagation loss.

The simulated mode profile of the 3D inverse-taper and the UHNA3 fiber Gaussian mode is shown in Fig. S7, resulting in a mode overlap of 92.0% for waveguide TE mode. The mode overlap factor is calculated using the following equation:

$$\eta = \left| \frac{\iint [E_{1y}^*(y, z)E_{2y}(y, z) + E_{1z}^*(y, z)E_{2z}(y, z)] dy dz}{\sqrt{\iint [|E_{1y}(y, z)|^2 + |E_{1z}(y, z)|^2] dy dz} \sqrt{\iint [|E_{2y}(y, z)|^2 + |E_{2z}(y, z)|^2] dy dz}} \right|^2. \quad (\text{S8})$$

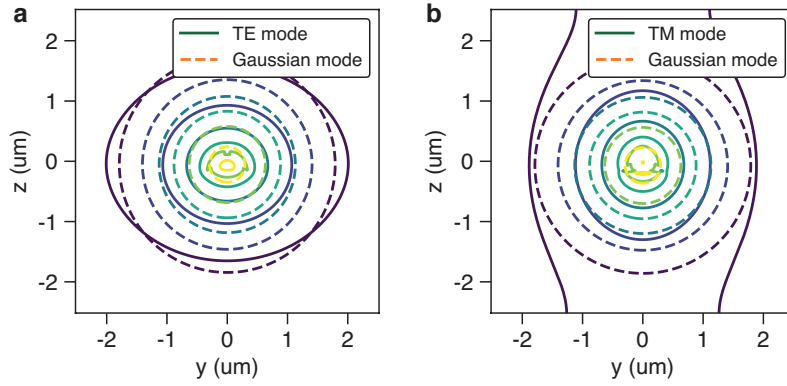


FIG. S7. **Optical mode profiles in the 3D inverse taper and UHNA3 fiber.** (a) Mode overlap between the 1030-nm TE mode of a 3D inverse-taper and that of UHNA3 fiber, with an overlap factor of 92.0%. A Gaussian mode with a mode field diameter of 2.6 μm was used to represent the mode profile in the UHNA3 fiber. (b) Mode overlap between the 1030-nm TM mode of a 3D inverse-taper and that of UHNA3 fiber, with an overlap factor of 87.9%.

S2.2. Rutherford backscattering spectrometry

We employ Rutherford backscattering spectrometry (RBS) to determine the film stoichiometry and Yb doping concentration. For the measurement, 2.45 MeV He^+ ions were used with a scattering angle of 170° . Simulations and fitting of the RBS spectrum were performed using SIMNRA by the authors. The measured spectrum, fitting, and calculated Yb density are shown in Fig. S8. In order to obtain an accurate profile of various elements over the entirety of the film thickness, a total of 11 layers were used to fit the RBS spectrum. One layer was used to represent the undoped AlO_x layer at the beginning of the growth (deepest), while the remaining 10 layers of similar thickness were used to represent the doped AlO_x region. The material composition and thickness of all layers were fine-tuned to achieve the best fit. A thick layer of stoichiometric SiO_2 was used underneath for the simulation, which matches the lower energy spectrum decently well. There is a trace amount of Ar within the film based on the simulation as expected, since Ar is the dominant sputtering gas used during the deposition process.

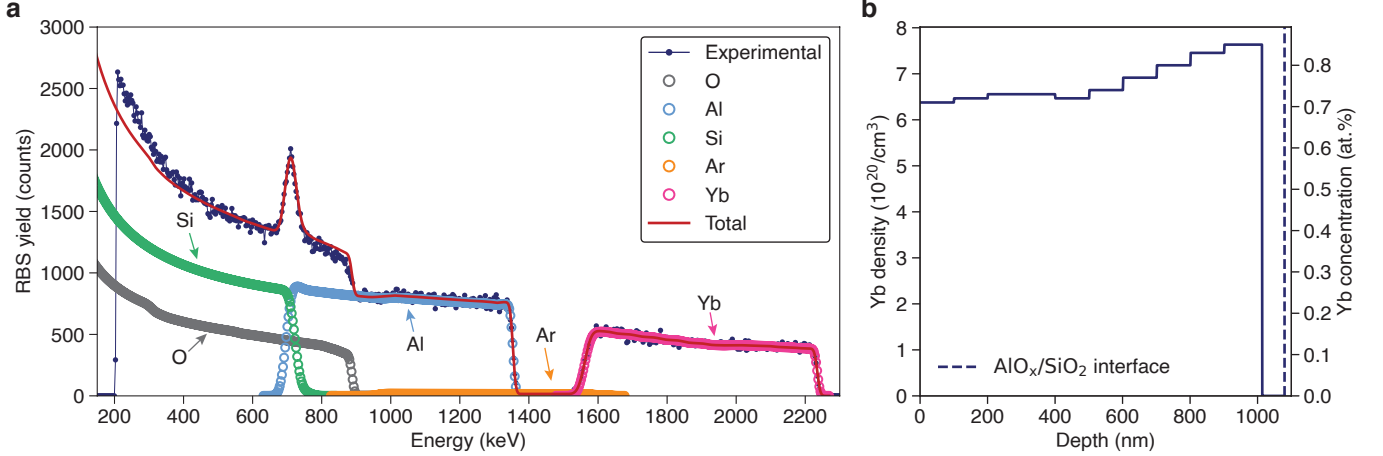


FIG. S8. **Rutherford backscattering spectrometry.** (a) Measured and simulated RBS spectra, individual element contributions are shown as separate traces. (b) Yb concentration depth profile.

Between the energy of 1550 keV and 2250 keV, the spectrum is dominated by the Yb scattering signal since it is the heaviest element in the film. With a large atomic number, Yb also has a large scattering cross-section. Consequently, even at concentrations as low as 0.7-0.8 at.% (atomic percentage), the He^+ counts scattered from Yb are comparable to those scattered from the Al and O. The high Yb sensitivity enables a highly accurate fit of the Yb concentration at different depths, as shown in Fig. S8b. At the low-energy edge near 1550 keV, the measured profile can be accurately reproduced by tuning the Yb concentration in the deepest layer and the Ar concentration near the surface. The best agreement is obtained for a gradual Ar profile near the surface, in which the atomic fraction increases from 0.1 at.% at the surface to 0.4 at.% in the deeper region. The location of this edge reflects the total areal atom density, since He^+ ions lose energy as they undergo scattering along their trajectory through the film. Accordingly, the minimum detected energy of He^+ ions scattered from Yb is determined by the total areal atomic density encountered by the ion beam, expressed in atom/cm^2 . This effect allows us to fit the total areal atom density of the film accurately.

After determining the Yb and Ar concentrations, the Al concentration in the top two thirds of the alumina film, corresponding to the 900–1400 keV region, is obtained by fitting the RBS signal. The O concentration in this upper portion of the film is then taken as the remaining atomic fraction not accounted for by the other elements. Extracting the Al concentration in the bottom third of the alumina film, corresponding to 700–900 keV, is more challenging because its signal overlaps with the oxygen contribution from the upper portion of the film. However, because the oxygen concentration in the top two thirds has already been determined, this overlapping contribution can be accounted for, allowing the Al concentration in the bottom third to be fitted. The O concentration in the bottom third is then again taken as the remaining atomic fraction not accounted for by the other elements. The total density previously determined from the Yb trace is then verified using the energy span of the Al scattering signal, which produces the sharp peak at 700 keV together with Si. We note that the minor discrepancies at low energies (below 400 keV) are a result of uncertainties in the stopping powers, which describe the rate of energy loss for He^+ ions as they travel through the material. These discrepancies do not affect the accuracy of our fitting, since none of the Al, Yb, and Ar signals appear in this range.

Following this high-to-low energy, element-by-element fitting procedure, we precisely determined the stoichiometry and total areal density of the AlO_x film. The O atomic fraction ranges between 61 at.% and 62 at.%, with an average of 61.5 at.%. The Al atomic fraction ranges from 36.8 at.% to 38.2 at.%, with an average of 37.4 at.%. This means

that the alumina ($\text{Al}_2\text{O}_{3.28}$) film is oxygen-rich. The average Yb atomic fraction within the doped region is 0.76 at.%, corresponding to an average density of 6.8×10^{20} atoms/cm³. The total number of atoms per unit area obtained from the fitting is 9.70×10^{18} at./cm². Combining the molar masses of Al, O, and Yb with the 1080 nm film thickness, we can calculate an average film density of 3.17 g/cm³ for the doped region and 2.99 g/cm³ for the undoped region. The Yb-related He^+ ion counts have a standard deviation of 19 counts, corresponding to a concentration uncertainty of 0.034 at.%. We therefore report the Yb concentration to a resolution of 0.01 at.%.

S2.3. Photoluminescence lifetime measurement

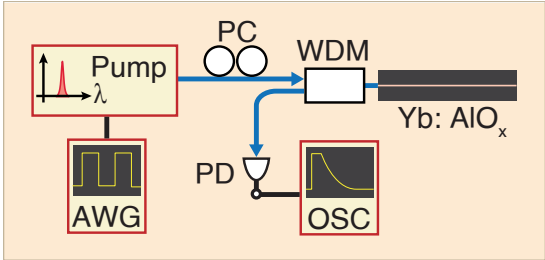


FIG. S9. Experimental setup for photoluminescence lifetime measurements.

The photoluminescence lifetime was measured by modulating a 976-nm pump coupled into a 6.6-mm-long waveguide. The resulting amplified spontaneous emission (ASE) was collected from the 1060-nm port of a WDM and detected with a Newport 1811 InGaAs photoreceiver. The electrical signal was recorded on a Keysight DSOX3014G oscilloscope in high-resolution mode to reduce noise, then fit with a single-exponential decay to extract the Yb lifetime. A low pump power of 3.7 mW was used to minimize quenching-induced lifetime shortening. The 976-nm pump was modulated at 10 Hz using the Thorlabs ITC4005 controller, with the modulation synchronized to the oscilloscope trigger.

S2.4. DFB laser characterization

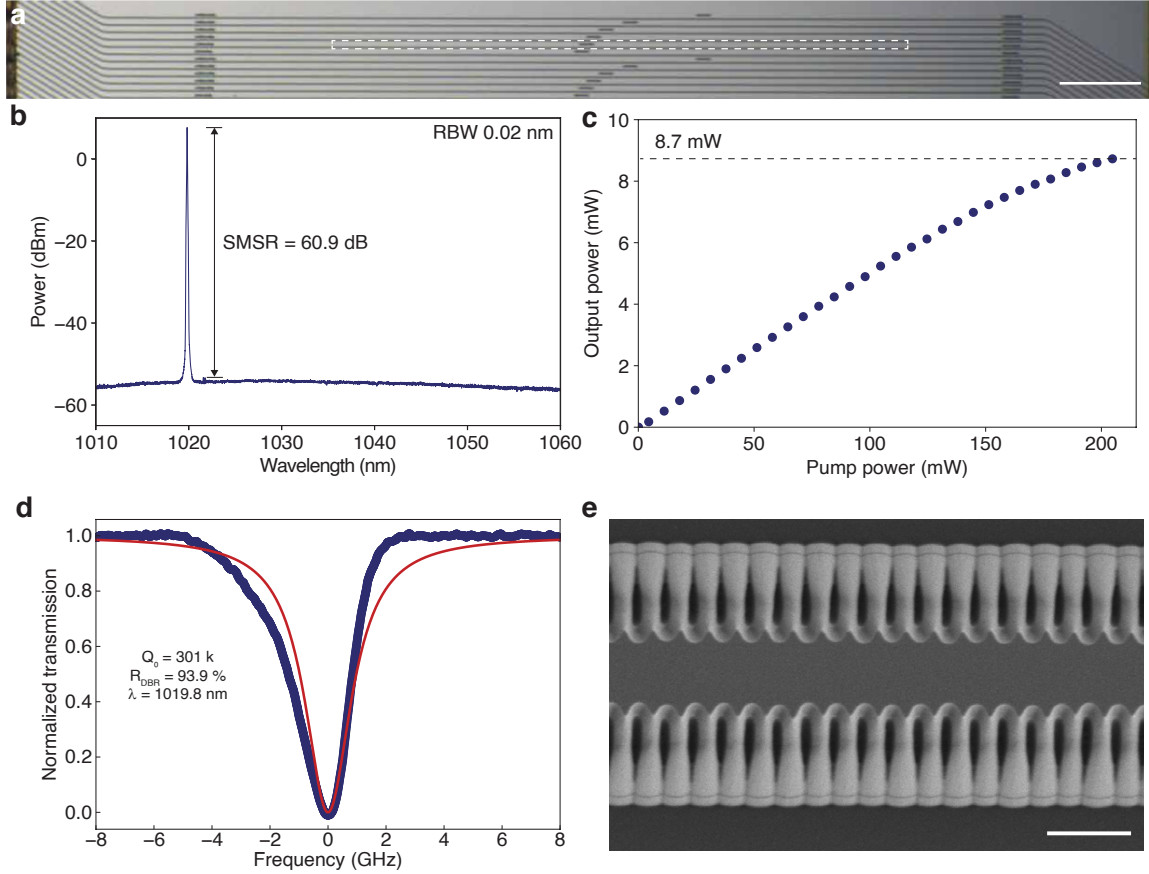


FIG. S10. **DFB laser characterization.** (a) Optical image of a DFB array. The DFB under test is highlighted. The scale bar is 500 μm . (b) DFB laser spectrum showing a side mode suppression ratio (SMSR) of 60.9 dB. A resolution bandwidth (RBW) of 0.02 nm was used for the measurement. (c) Measured output power at 1019.8 nm. (d) Measured and fitted reflection spectra of the DFB laser cavity showing a Bragg mirror reflectivity of 93.9%. (e) SEM image of a section of the Bragg mirror. The scale bar is 1 μm .

We demonstrate a DFB laser formed by two 1.6-mm-long Bragg gratings, each with a width of 1.4 μm (before lateral etch offset) and 100 nm peak-to-peak sidewall corrugations, separated by a 60 μm cavity. When pumped unidirectionally at 976 nm, the device produces a maximum on-chip output power of 8.7 mW at 1019.8 nm and exhibits a side-mode suppression ratio as high as 60.9 dB. The output was collected with 1064 nm lensed fibers (TSMJ-3A-1064-6/125/-0.25-10-2-10-1) and characterized through a 980/1060 nm fiber wavelength-division multiplexer using a Yokogawa AQ6375 optical spectrum analyzer with a 0.02-nm resolution bandwidth. To suppress facet reflections, the output waveguides were angled by 32°.

S2.5. Optical gain and noise figure measurement

The noise figure (NF) was calculated using the input and output laser spectra acquired by an optical spectrum analyzer (Yokogawa AQ6370D). Fig. S11 shows the input and output spectra for the lowest noise figure of 3.3 dB. For the NF calculations, we used the following definition [SI16] which includes the 1/G shot noise and subtracts the input laser's source spontaneous emission (SSE):

$$F = \frac{P_{\text{ASE, out}} - GP_{\text{SSE}}}{G h \nu B_0} + \frac{1}{G}. \quad (\text{S9})$$

Here, $P_{\text{ASE,out}}$ and P_{SSE} are the output ASE and input SSE powers respectively, G is the optical gain, h is Planck's constant, ν is the peak frequency, B_0 is the effective noise bandwidth, and F denotes the noise figure. To ensure accurate power scaling, the OSA bin power was normalized with the Thorlabs S145C power monitor and the effective noise bandwidth was calibrated to a value of 0.144 nm. We treat the measured ASE power as the combined ASE contribution from both polarizations due to the similar fiber-mode overlap factors (section S2.1). The minimum measured on-chip noise figure of 3.3 dB is enabled by the low spontaneous emission factor (n_{sp}), which is given by

$$\begin{aligned}\eta &= \sigma_{21,s}/\sigma_{12,s}, \\ n_{sp} &= \frac{\eta N_2}{\eta N_2 - N_1}, \\ \text{NF}_{min} &= 2n_{sp}.\end{aligned}\tag{S10}$$

Setting $N_2 = N_1$ due to equal pump emission and absorption cross sections for the pump yields a minimum noise figure of 3.29 dB using the cross sections obtained in section S1.1. An n_{sp} value of 1 corresponds to the quantum limited 3 dB noise figure.

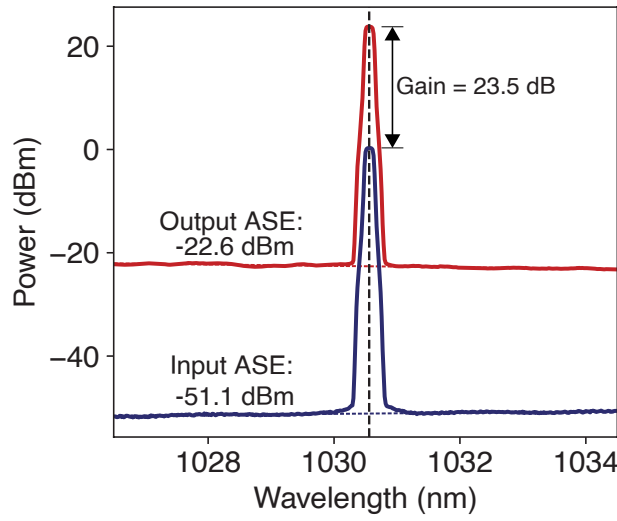


FIG. S11. Optical spectra of the on-chip input and amplified output signals used to calculate the lowest noise figure of 3.3 dB.

In this paper, we assume equal coupling losses at the input and output facets of the amplifier. However, at a pump power of 52.7 mW, the ASE measured from the input side was about 2.5 dB higher than that measured from the output side. This suggests that the input coupling loss is lower than the assumed 1.0 dB per facet. As a result, the actual noise figure is likely higher than the calculated value of 3.3 dB assuming symmetric facet coupling loss.

S2.6. Device performance comparison

Table S1 shows a comparison of CW amplifiers with integrated rare-earth gain, transition-metal gain, rare-earth fibers, and III-V amplifiers. Table S2 shows a comparison of pulse amplifiers. The 730 nJ saturation energy of the Yb:AlO_x gain platform is advantageous compared to III-V SOAs with lower saturation energies of 5–10 pJ [SI17] and shorter carrier lifetimes on the order of 100 ps [SI17]. For pulse energies above the saturation energy, the beginning of the pulse will experience higher gain than the tail of the pulse. Additionally, the change in carrier populations creates an index shift, resulting in an effective n_2 coefficient on the order of $n_2 = 1 \times 10^{-13} \text{ m}^2/\text{W}$ [SI17], which is around 5–6 orders of magnitude larger than the alumina platform.

TABLE S1. Integrated CW Amplification

Active Medium	WL (nm)	Output (W)	Eff. (%)	On-chip gain (dB)	Off-chip gain (dB)	NF (dB)	Reference
Yb:AlO _x	1030	0.590	71	28.6	26.6	3.3	This work
Ti:Sapphire	790	~0.06	12.3	~25	-	-	[SI18]
Yb:AlO _x	1020	-	-	2.5	-	-	[SI1]
Yb:LNOI	1060	-	5	8	-10	-	[SI19]
Yb:LNOI	1064	7.94×10 ⁻⁹	-	9	-1.72	-	[SI20]
Nd:Al ₂ O ₃	1064	2.2×10 ⁻³	1.4	19.9	14.5	8.5	[SI21]
Nd:Al ₂ O ₃	1064	2.75×10 ⁻⁴	-	14.4	-	-	[SI22]
Nd:Al ₂ O ₃	1330	3.23×10 ⁻⁵	-	5.1	-	-	[SI22]
Er:Si ₃ N ₄ ^a	1550	0.145	60	30	24	7	[SI3]
Er:Si ₃ N ₄	1550	0.022	12	15	5.2	-	[SI23]
Er:Si ₃ N ₄	1560	0.055	-	29.8	24	-	[SI24]
Er:Si ₃ N ₄	1550	2.3×10 ⁻³	-	-	12	-	[SI25]
Er:Si ₃ N ₄	1560	0.241	28.4	16	13.5	-	[SI26]
Er:Yb:LNOI ^b	1531	1.2×10 ⁻⁷	-	8.26	-	-	[SI27]
Er:Yb:LNOI	1532	4.07×10 ⁻⁴	-	27	10	-	[SI28]
Er:LNOI	1532	0.036	-	38	24.6	-	[SI29],[SI30]
Er:LNOI	1533	0.063	-	35	-	-	[SI31]
Er:LNOI	1531	4.0×10 ⁻⁵	-	6	-	4.2	[SI32]
Er:Ta ₂ O ₅	1532	-	-	4.8	-	-	[SI33],[SI34]
Er:Ga ₂ O ₃	1532	1.7×10 ⁻⁷	-	4.7	-	-	[SI35]
Er:Al ₂ O ₃ ^c	1533	1.3×10 ⁻⁷	-	6.27	-1.23	-	[SI36]
Er:Al ₂ O ₃ ^d	1532	2.51×10 ⁻³	-	20	0	-	[SI37]
Er:Al ₂ O ₃	1556	0.088	16.3	28.5	24.3	4.6	[SI38]
Er:Al ₂ O ₃	1531	0.021	-	33.5	-16.5	-	[SI39]
Er:glass	1536	2.8×10 ⁻⁷	-	6.5	4.5	-	[SI40]
Er:Al ₂ O ₃ on SiN	1533	7.9×10 ⁻⁷	-	1.98	-	-	[SI41]
Er:Al ₂ O ₃ on SiN	1532	6.3×10 ⁻⁵	-	18.1	-1.9	-	[SI42]
Er:Al ₂ O ₃ on SiN	1560	23.5×10 ⁻³	-	16.33	13.73	~3.1	[SI43]
Er:Yb:Al ₂ O ₃	1531	1.41×10 ⁻⁴	-	4.3	-4.7	-	[SI44]
Er:TeO ₂	1530	0.02	-	14	3	-	[SI45]
Er:TeO ₂ on SiN	1558	3.2×10 ⁻⁵	-	5	-	-	[SI46]
Tm:TeO ₂ on SiN	1870	7.6×10 ⁻⁵	-	7.8	-4.2	-	[SI47]
Tm:Al ₂ O ₃ on SiN	1850	~1-1.8	63-66	16.5	11.2	5	[SI48],[SI49]
Tm:Al ₂ O ₃ on SiN	1879	0.815	43	30	22	3.7	[SI50]
Yb:fiber	-	4.8	75	-	-	-	Thorlabs ^e
Yb:fiber	1050	0.35	-	-	29	5.3	Thorlabs ^f
III-V MQW on Si ^g	1570	0.013	-	13	3	5	[SI51],[SI52]
III-V MQW on Si	1550	0.048	-	25.5	7.5	-	[SI53]
III-V MQW on Si	1575	0.056	-	27	8	~9	[SI54]
III-V MQW on Si	2001	3.16×10 ⁻⁵	-	12	-	-	[SI55]
III-V MQW	1560	4×10 ⁻³	-	20	-	-	[SI56]
III-V QD ^h	1300	0.01	-	16	-	-	[SI57]
III-V QD	1300	8×10 ⁻³	-	18	-6	8	[SI58]
III-V QD on Si ⁱ	1315	0.229	-	39	26.9	8.5	[SI59]
III-V QD	1305	0.087	-	18.2	-	5.6	[SI60]
III-V QD	1450	0.2	-	25	-	5	[SI61]
III-V QD	1450	0.016	-	18	-	5.6	[SI62]
III-V QD	1510	0.052	-	37	22.5	9	[SI63]
III-V TSA ^j	780	0.5	-	-	20	-	[SI64]
III-V MQW μTP SiN ^k	1570	7.6×10 ⁻³	-	14	-	10.6	[SI65]
III-V μTP on Si	1550	3.1×10 ⁻⁴	-	8.1	-	-	[SI66]
III-V MQW μTP on Si	1573	0.079	-	9	-	-	[SI67]
BOA ^l	1040	> 69×10 ⁻³	-	-	28	7.5	Thorlabs ^m

^a Er implanted in Si₃N₄ waveguides. ^b LNOI: lithium niobate on insulator. ^c Ge₂₅Sb₁₀S₆₅ waveguides on Er:Al₂O₃ deposited by atomic layer deposition (ALD). ^d Fully-etched Er:Al₂O₃ amplifier waveguides heterogeneously integrated with Si₃N₄ photonic circuits. ^e Model number: YB1200-6/125DC. ^f Model number: YDFA300P. ^g MQW: multi-quantum well. III-V bonded on Si unless otherwise specified. ^h QD: quantum dot. ⁱ Directly epitaxially grown on Si. ^j TSA: tapered semiconductor amplifier. ^k μTP: micro-transfer print. ^l BOA: booster optical amplifier. ^m Model number: BOA1050S.

TABLE S2. Integrated Ultrafast Pulse Amplification

Active Medium	WL (nm)	Pulse energy (nJ)	Input width (ps)	Rep. rate (MHz)	On-chip gain (dB)	Reference
Yb:AlO _x	1050	5.3	5.2	83.3	18.9	This work
Ti:Sapphire	800	2.3	2.2	1.25	17.0	[SI18]
Tm:Al ₂ O ₃	1815	0.095	2.5	1,000	17	[SI68]
Er:Si ₃ N ₄	1558	0.131	-	100	24	[SI3]
Er:Ta ₂ O ₅	1550	7.1×10^{-4}	38	6,000	3.8	[SI69]
Cr:ZnS CPA ^a	2336	33.6	500	70	18.8	[SI70]
III-V TSA ^b	780	1.78	150	100	20	[SI64]
III-V QD TSA	1260	~ 0.062	1.37	16,000	~ 22	[SI71]
III-V SOA ^c	835	0.043	-	323	-	[SI72]
III-V cascaded SOA XCPA ^d	975	238	6,480	57	41 (cascaded)	[SI73],[SI74]

^a CPA: chirped pulse amplification. Depressed cladding buried waveguide in Cr-doped ZnS crystal on Si, inscribed by pulse laser direct writing. ^b TSA: tapered semiconductor amplifier. ^c SOA: semiconductor optical amplifier. ^d XCPA: extreme chirped pulse amplification. Multiple SOAs were cascaded.

-
- [SI1] Loiko, P. *et al.* Quantitative analysis of cooperative upconversion in Al_2O_3 : Yb^{3+} . *Optical Materials* **162**, 116798 (2025).
- [SI2] Alimov, O. K. *et al.* Investigations of Yb-doped optical fiber using selective laser excitation. *Applied Physics B* **104** (2011).
- [SI3] Liu, Y. *et al.* A photonic integrated circuit-based erbium-doped amplifier. *Science* **376**, 1309–1313 (2022).
- [SI4] Purnawirman *et al.* C- and L-band erbium-doped waveguide lasers with wafer-scale silicon nitride cavities. *Optics Letters* **38**, 1760–1762 (2013).
- [SI5] Desurvire, E. *Erbium-Doped Fiber Amplifiers: Principles and Applications* (John Wiley & Sons, New York, 1994).
- [SI6] Agazzi, L. *Spectroscopic excitation and quenching processes in rare-earth-ion-doped Al_2O_3 and their impact on amplifier and laser performance*. Ph.D. thesis, University of Twente (2012).
- [SI7] Kik, P. & Polman, A. Cooperative upconversion as the gain-limiting factor in Er-doped miniature Al_2O_3 optical waveguide amplifiers. *Journal of Applied Physics* **93**, 5008–5012 (2003).
- [SI8] Worhoff, K. *et al.* Reliable low-cost fabrication of low-loss Al_2O_3 waveguides with 5.4-dB optical gain. *IEEE Journal of Quantum Electronics* **45**, 454–461 (2009).
- [SI9] Zeng, T. *et al.* Injection locking of integrated erbium-based laser. In *CLEO: Applications and Technology* (2025).
- [SI10] Bradley, J., Ay, F., Wörhoff, K. & Pollnau, M. Fabrication of low-loss channel waveguides in Al_2O_3 and Y_2O_3 layers by inductively coupled plasma reactive ion etching. *Applied Physics B* **89**, 311–318 (2007).
- [SI11] Hu, Y. *et al.* Kramers–Kronig causality in integrated photonics: The spectral tension between ultraviolet transition and mid-infrared absorption. *arXiv preprint arXiv:2603.28676* (2026).
- [SI12] Coherent, Inc. *Ultra-High NA Single-Mode Fibers*. Coherent, Inc. (2020). Datasheet NU0019.
- [SI13] Lamee, K. F., Carlson, D. R., Newman, Z. L., Yu, S.-P. & Papp, S. B. Nanophotonic tantalum waveguides for supercontinuum generation pumped at 1560 nm. *Optics Letters* **45**, 4192–4195 (2020).
- [SI14] Jung, H. *et al.* Tantalum Kerr nonlinear integrated photonics. *Optica* **8**, 811–817 (2021).
- [SI15] Carollo, A. R. *et al.* Amorphous metal oxide mixtures for high-Q integrated nonlinear photonics. *arXiv preprint arXiv:2508.14887* (2025).
- [SI16] Haus, H. The noise figure of optical amplifiers. *IEEE Photonics Technology Letters* **10**, 1602–1604 (1998).
- [SI17] Agrawal, G. P. & Olsson, N. A. Self-phase modulation and spectral broadening of optical pulses in semiconductor laser amplifiers. *IEEE Journal of Quantum Electronics* **25**, 2297–2306 (1989).
- [SI18] Yang, J. *et al.* Titanium: sapphire-on-insulator integrated lasers and amplifiers. *Nature* **630**, 853–859 (2024).
- [SI19] Zhang, Z. *et al.* On-chip integrated Yb_{3+} -doped waveguide amplifiers on thin film lithium niobate. *Micromachines* **13** (2022).
- [SI20] Zhang, Y. *et al.* On-chip ytterbium-doped lithium niobate waveguide amplifiers with high net internal gain. *Optics Letters* **48**, 1810–1813 (2023).
- [SI21] Jongebloed, B., Osornio-Martinez, C., Wang, K., Dijkstra, M. & García-Blanco, S. Fiber-to-fiber gain in Nd-doped aluminium oxide waveguide amplifiers. *Optics Express* **34**, 4522–4534 (2026).
- [SI22] Yang, J., van Dalen, K., Worhoff, K., Ay, F. & Pollnau, M. High-gain Al_2O_3 :Nd $_{3+}$ channel waveguide amplifiers at 880 nm, 1060 nm, and 1330 nm. *Applied Physics B* **101**, 119–127 (2010).
- [SI23] Qiu, Z. *et al.* Hybrid integrated multi-lane erbium-doped Si_3N_4 waveguide amplifiers. In *ECOC 2024; 50th European Conference on Optical Communication*, 1721–1724 (VDE, 2024).
- [SI24] Che, D. *et al.* Terabit-class coherent communications enabled by an integrated photonics erbium-doped amplifier. *arXiv preprint arXiv:2412.07627* (2024).
- [SI25] Yang, X. *et al.* A polarization insensitive erbium-doped waveguide amplifier. In *2025 Conference on Lasers and Electro-Optics (CLEO)*, 1–2 (IEEE, 2025).
- [SI26] Qiu, Z. *et al.* Scalable-manufactured erbium-doped silicon nitride amplifiers with high output power. In *2025 Conference on Lasers and Electro-Optics (CLEO)*, 1–2 (IEEE, 2025).
- [SI27] Zhang, Y. *et al.* Highly efficient on-chip erbium–ytterbium co-doped lithium niobate waveguide amplifiers. *Photonics Research* **11**, 1733–1737 (2023).
- [SI28] Zhang, Z. *et al.* Erbium–ytterbium co-doped thin-film lithium niobate integrated waveguide amplifier with a 27 dB internal net gain. *Optics Letters* **48**, 4344–4347 (2023).
- [SI29] Wang, Y. *et al.* Erbium-doped lithium niobate on insulator waveguide amplifier with ultra-high internal net gain of 38 dB. In *2024 Conference on Lasers and Electro-Optics (CLEO)*, 1–2 (IEEE, 2024).
- [SI30] Wang, Y. *et al.* Unifying optical gain and electro-optical dynamics in Er-doped thin-film lithium niobate platform. *Nature Communications* **16**, 10462 (2025).
- [SI31] Wang, C. *et al.* A large-mode-area erbium-doped waveguide amplifier with more than 18 dBm output power. In *2025 Conference on Lasers and Electro-Optics (CLEO)*, 1–2 (IEEE, 2025).
- [SI32] Xiong, N. *et al.* On-chip net-amplified modulator in erbium-doped thin-film lithium niobate with 110-GHz bandwidth. *Photonics Research* **14**, 2140–2148 (2026).
- [SI33] Subramanian, A. Z., Murugan, G. S., Zervas, M. N. & Wilkinson, J. S. Spectroscopy, modeling, and performance of erbium-doped Ta_2O_5 waveguide amplifiers. *Journal of Lightwave Technology* **30**, 1455–1462 (2012).
- [SI34] Subramanian, A. Z., Murugan, G. S., Zervas, M. N. & Wilkinson, J. S. High index contrast Er: Ta_2O_5 waveguide amplifier on oxidised silicon. *Optics Communications* **285**, 124–127 (2012).

- [SI35] Liu, R. *et al.* Erbium-doped Ga₂O₃ waveguide for optical amplification. *Applied Physics Letters* **123** (2023).
- [SI36] Wang, C. *et al.* High-gain waveguide amplifiers in Ge₂₅Sb₁₀Se₆₅ photonics heterogeneous integration with erbium-doped Al₂O₃ thin films. *Laser & Photonics Reviews* **18**, 2300893 (2024).
- [SI37] Vázquez-Córdova, S. A. *et al.* Erbium-doped spiral amplifiers with 20 dB of net gain on silicon. *Optics Express* **22**, 25993–26004 (2014).
- [SI38] Osornio-Martinez, C., Bonneville, D., Dijkstra, M., do Nascimento Jr, A. & García-Blanco, S. Broadband packaged erbium-doped polycrystalline Al₂O₃ waveguide amplifier with 24 dB external net gain. *Optics Express* **33**, 28985–28994 (2025).
- [SI39] Bonneville, D., Osornio-Martinez, C., Dijkstra, M. & García-Blanco, S. High on-chip gain spiral Al₂O₃: Er₃₊ waveguide amplifiers. *Optics Express* **32**, 15527–15536 (2024).
- [SI40] Ghosh, R. N. *et al.* 8-mw threshold Er³⁺-doped planar waveguide amplifier. *IEEE Photonics Technology Letters* **8**, 518–520 (1996).
- [SI41] Rönn, J. *et al.* Ultra-high on-chip optical gain in erbium-based hybrid slot waveguides. *Nature Communications* **10**, 432 (2019).
- [SI42] Mu, J., Dijkstra, M., Korterik, J., Offerhaus, H. & García-Blanco, S. M. High-gain waveguide amplifiers in Si₃N₄ technology via double-layer monolithic integration. *Photonics Research* **8**, 1634–1641 (2020).
- [SI43] Osornio-Martinez, C. *et al.* Monolithically integrated erbium-doped polycrystalline Al₂O₃ waveguide amplifier on silicon photonics platform. *Optics Express* **33**, 23491–23502 (2025).
- [SI44] Bonneville, D. B., Frankis, H. C., Wang, R. & Bradley, J. D. Erbium-ytterbium co-doped aluminium oxide waveguide amplifiers fabricated by reactive co-sputtering and wet chemical etching. *Optics Express* **28**, 30130–30140 (2020).
- [SI45] Vu, K. & Madden, S. Tellurium dioxide erbium-doped planar rib waveguide amplifiers with net gain and 2.8 dB/cm internal gain. *Optics Express* **18**, 19192–19200 (2010).
- [SI46] Frankis, H. C. *et al.* Erbium-doped TeO₂-coated Si₃N₄ waveguide amplifiers with 5 dB net gain. *Photonics Research* **8**, 127–134 (2020).
- [SI47] Kiani, K. M. *et al.* Thulium-doped tellurium oxide waveguide amplifier with 7.6 dB net gain on a silicon nitride chip. *Optics Letters* **44**, 5788–5791 (2019).
- [SI48] Singh, N. *et al.* Watt-class silicon photonics-based optical high-power amplifier. *Nature Photonics* **19**, 307–314 (2025).
- [SI49] Singh, N. *et al.* Sub-2W tunable laser based on silicon photonics power amplifier. *Light: Science & Applications* **14**, 18 (2025).
- [SI50] Lorenzen, J., Singh, N., Wang, K., García-Blanco, S. M. & Kärtner, F. X. Silicon photonics LMA amplifiers: High power, high gain, low noise and tunable polarization sensitivity. *arXiv preprint arXiv:2505.15361* (2025).
- [SI51] Park, H., Fang, A. W., Bowers, J. E., Jones, R. & Cohen, O. An electrically pumped hybrid silicon evanescent amplifier. In *OFC/NFOEC 2007-2007 Conference on Optical Fiber Communication and the National Fiber Optic Engineers Conference*, 1–3 (IEEE, 2007).
- [SI52] Park, H. *et al.* A hybrid AlGaInAs–silicon evanescent amplifier. *IEEE Photonics Technology Letters* **19**, 230–232 (2007).
- [SI53] Davenport, M. L. *et al.* Heterogeneous silicon/III–V semiconductor optical amplifiers. *IEEE Journal of Selected Topics in Quantum Electronics* **22**, 78–88 (2016).
- [SI54] Van Gasse, K., Wang, R. & Roelkens, G. 27 dB gain III–V-on-silicon semiconductor optical amplifier with >17 dBm output power. *Optics Express* **27**, 293–302 (2019).
- [SI55] Volet, N. *et al.* Semiconductor optical amplifiers at 2.0- μ m wavelength heterogeneously integrated on silicon. In *CLEO: Science and Innovations*, SM4G–4 (Optica Publishing Group, 2016).
- [SI56] Li, X., Adams, M., Alexandropoulos, D. & Lealman, I. Gain recovery in semiconductor optical amplifiers. *Optics Communications* **281**, 3466–3470 (2008).
- [SI57] Akiyama, T., Hatori, N., Nakata, Y., Ebe, H. & Sugawara, M. Pattern-effect-free amplification and cross-gain modulation achieved by using ultrafast gain nonlinearity in quantum-dot semiconductor optical amplifiers. *Physica Status Solidi (b)* **238**, 301–304 (2003).
- [SI58] Bakonyi, Z. *et al.* High-gain quantum-dot semiconductor optical amplifier for 1300 nm. *IEEE Journal of Quantum Electronics* **39**, 1409–1414 (2003).
- [SI59] Liu, S. *et al.* High-performance O-band quantum-dot semiconductor optical amplifiers directly grown on a CMOS-compatible silicon substrate. *ACS Photonics* **6**, 2523–2529 (2019).
- [SI60] St-Arnault, C. *et al.* Performance and characterization comparison of QD SOA, QW SOA, bulk SOA and PDFA for multi-Tbps O-band WDM links. *Journal of Lightwave Technology* **43**, 1915–1925 (2025).
- [SI61] Akiyama, T. *et al.* An ultrawide-band semiconductor optical amplifier having an extremely high penalty-free output power of 23 dBm achieved with quantum dots. *IEEE Photonics Technology Letters* **17**, 1614–1616 (2005).
- [SI62] Sekiguchi, S. *et al.* Highly efficient columnar-quantum-dot semiconductor optical amplifier in high temperature condition. In *Optical Fiber Communication Conference, OThK4* (Optica Publishing Group, 2010).
- [SI63] Kim, N. *et al.* Gain characteristics of InAs/InGaAsP quantum dot semiconductor optical amplifiers at 1.5 μ m. *Applied Physics Letters* **90** (2007).
- [SI64] Cruz, F. C., Stowe, M. C. & Ye, J. Tapered semiconductor amplifiers for optical frequency combs in the near infrared. *Optics Letters* **31**, 1337–1339 (2006).
- [SI65] Op de Beeck, C. *et al.* Heterogeneous III-V on silicon nitride amplifiers and lasers via microtransfer printing. *Optica* **7**, 386–393 (2020).
- [SI66] Qin, S. *et al.* Micro-transfer printing of InP SOAs on advanced silicon photonics platform for C-band pre-amplified receivers. In *Silicon Photonics XX*, vol. 13371, 111–115 (SPIE, 2025).

- [SI67] Soltanian, E. *et al.* Micro-transfer-printed III-V-on-Si semiconductor optical amplifier with 15 dBm output saturation power. In *2023 IEEE Silicon Photonics Conference (SiPhotonics)*, 1–2 (IEEE, 2023).
- [SI68] Gaafar, M. A. *et al.* Femtosecond pulse amplification on a chip. *Nature Communications* **15**, 8109 (2024).
- [SI69] Vaid, H. *et al.* On-Chip Er: Ta₂O₅ optical pulse amplifier. *Optical Materials* **166**, 117184 (2025).
- [SI70] Rudenkov, A. *et al.* Chirped pulse waveguide amplifier. *Optics Express* **33**, 28935–28946 (2025).
- [SI71] Weber, C. *et al.* Picosecond pulse amplification up to a peak power of 42 W by a quantum-dot tapered optical amplifier and a mode-locked laser emitting at 1.26 μm . *Optics Letters* **40**, 395–398 (2015).
- [SI72] Resan, B., Archundia, L. & Delfyett, P. J. FROG measured high-power 185-fs pulses generated by down-chirping of the dispersion-managed breathing-mode semiconductor mode-locked laser. *IEEE Photonics Technology Letters* **17**, 1384–1386 (2005).
- [SI73] Kim, K., Lee, S. & Delfyett, P. J. 1.4 kW high peak power generation from an all semiconductor mode-locked master oscillator power amplifier system based on extreme chirped pulse amplification (X-CPA). *Optics Express* **13**, 4600–4606 (2005).
- [SI74] Kim, K., Lee, S. & Delfyett, P. J. Generation of 238 nJ, 16 ns stretched pulses in all semiconductor X-CPA system. In *The 17th Annual Meeting of the IEEE Lasers and Electro-Optics Society, 2004. LEOS 2004.*, vol. 2, 731–732 (IEEE, 2004).